Evolutionary Map of the Universe (EMU): Compact radio sources in the Scorpio field towards the Galactic plane

S. Riggi[1]⋆, G. Umana[1], C. Trigilio[1], F. Cavallaro[11,1], A. Ingallinera[1], P. Leto[1], F. Bufano[1], R.P. Norris[2,3], A.M. Hopkins[4,2], M.D. Filipović[2], H. Andernach[5], J.Th. van Loon[6], M. J. Michałowski[7], C. Bordiu[1,8], T. An[9], C. Buemi[1], E. Carretti[10], J.D. Collier[11,2], T. Joseph[12], B.S. Koribalski[3,2], R. Kothes[13], S. Loru[1], D. McConnell[3], M. Pommier[14], E. Sciacca[1], F. Schillirò[1], F. Vitello[10], K. Warhurst[15] and M. Whiting[3]

[1] *INAF-Osservatorio Astrofisico di Catania, Via Santa Sofia 78, 95123 Catania, Italy*
[2] *School of Science, Western Sydney University, Locked Bag 1797, Penrith, NSW 2751, Australia*
[3] *CSIRO Astronomy & Space Science, P.O. Box 76, Epping, NSW 1710, Australia*
[4] *Australian Astronomical Optics, Macquarie University, 105 Delhi Rd, North Ryde, NSW 2113, Australia*
[5] *Depto. de Astronomía, DCNE, Universidad de Guanajuato, Cjón. de Jalisco, Col. Valenciana, Guanajuato, CP 36023, Mexico*
[6] *Lennard-Jones Laboratories, Keele University, ST5 5BG, UK*
[7] *Astronomical Observatory Institute, Faculty of Physics, Adam Mickiewicz University, ul. Słoneczna 36, 60-286 Poznań, Poland*
[8] *Centro de Astrobiología (INTA-CSIC), Ctra. M-108, km. 4, 28850 Torrejón de Ardoz, Madrid, Spain*
[9] *Shanghai Astronomical Observatory, Chinese Academy of Sciences, 80 Nandan Road, Shanghai, 200030, China*
[10] *INAF Istituto di Radioastronomia, Via Gobetti 101, 40129 Bologna, Italy*
[11] *The Inter-University Institute for Data Intensive Astronomy (IDIA), Department of Astronomy, University of Cape Town, Rondebosch, 7701, South Africa*
[12] *School of Physics and Astronomy, University of Manchester, Oxford Road, Manchester, M13 9PL, UK*
[13] *Dominion Radio Astrophysical Observatory, Herzberg Astronomy and Astrophysics, National Research Council Canada, PO Box 248, Penticton, BC V2A 6J9, Canada*
[14] *Univ Lyon, Univ Lyon1, Ens de Lyon, CNRS, Centre de Recherche Astrophysique de Lyon UMR5574, 9 av Charles Andé F- 69230, Saint-Genis-Laval, France*
[15] *CSIRO Astronomy & Space Science, 33 Onslow St, Geraldton, WA 6530. Australia*

Accepted XXX. Received YYY; in original form ZZZ

ABSTRACT

We present observations of a region of the Galactic plane taken during the Early Science Program of the Australian Square Kilometre Array Pathfinder (ASKAP). In this context, we observed the Scorpio field at 912 MHz with an uncompleted array consisting of 15 commissioned antennas. The resulting map covers a square region of ∼40 deg^2, centred on (l, b)=(343.5°,0.75°), with a synthesized beam of 24"×21" and a background rms noise of 150-200 μJy/beam, increasing to 500-600 μJy/beam close to the Galactic plane. A total of 3963 radio sources were detected and characterized in the field using the caesar source finder. We obtained differential source counts in agreement with previously published data after correction for source extraction and characterization uncertainties, estimated from simulated data. The ASKAP positional and flux density scale accuracy were also investigated through comparison with previous surveys (MGPS, NVSS) and additional observations of the Scorpio field, carried out with ATCA at 2.1 GHz and 10" spatial resolution. These allowed us to obtain a measurement of the spectral index for a subset of the catalogued sources and an estimated fraction of (at least) 8% of resolved sources in the reported catalogue. We cross-matched our catalogued sources with different astronomical databases to search for possible counterparts, finding ∼150 associations to known Galactic objects. Finally, we explored a multiparametric approach for classifying previously unreported Galactic sources based on their radio-infrared colors.

Key words: radio continuum: general – catalogues – surveys – Galaxy: general – techniques: interferometric – techniques: image processing

⋆ E-mail: simone.riggi@inaf.it

1 INTRODUCTION

The next-generation deep radio continuum surveys, such as the Evolutionary Map of the Universe (EMU) (Norris et al. 2011), planned at the Australian SKA Pathfinder (ASKAP) telescope (Johnston et al. 2008) will open a new era in radio astronomy with potential new discoveries expected in several fields, from Galaxy evolution and characterization to Galactic Science.

In the full-operational mode, the ASKAP telescope is made of 36 12-metre antennas installed in Western Australia, each one equipped with a Phased Array Feed (PAF) receiver (Schinckel et al. 2012), operating with a bandwidth of 288 MHz over the frequency range 700-1800 MHz. The PAF system forms 36 beams and provides an instantaneous field of view of ∼30 square degrees, allowing ASKAP to survey the southern sky with unprecedented speed (∼220 deg^2 per hour at a target 1σ rms of 100 μJy/beam) and higher resolution (∼10" at 950 MHz) compared to existing surveys.

The array has a maximum baseline of 6 km and was completed in mid 2019. During the commissioning phase, the ASKAP EMU Early Science Program (ESP) was launched (October 2017), in which several target fields were observed with the aim of validating the array operations, the observation strategy and the data reduction pipeline. During this preparatory phase, it became evident that the imaging performance exceeded those of past observations, enabling valid scientific results even with an incomplete array. The Scorpio field was the first Galactic field observed during the ASKAP ESP using 15 commissioned antennas (Umana et al. in prep.).

The Scorpio survey (Umana et al. 2015) started in 2011 with multiple scientific goals. The original objectives were the study and characterization of different types of Galactic radio sources, with a focus on radio stars and circumstellar regions (e.g. HII regions). Recently, the study and characterization of stellar relics, such as Galactic supernova remnants (SNRs) in connection with observations at different wavelengths (infrared and gamma-ray primarily) has become an additional target of interest (Ingallinera et al. 2017). The survey also represents an important testbench for the ASKAP data reduction pipeline in the Galactic plane and for the analysis methods designed for the upcoming EMU survey.

This paper is the second of a series of works planned with ASKAP Scorpio Early Science data. In the first paper (Umana et al. in prep.) we discuss the ASKAP's potential for the discovery of different classes of Galactic objects in comparison with original ATCA observations, and described the data reduction strategies adopted to produce the final mosaic. The goal of this paper is to report a first catalogue of the compact sources present in Scorpio. This work will also serve as a validation on real data of the designed source extraction algorithms tested so far with simulated data (Riggi et al. 2016, 2019).

The paper is organized as follows. The ASKAP Scorpio radio observations and data reduction are briefly described in Section 2. In Section 3 we describe the source extraction methodologies used to build the source catalogue, and discuss the typical performance achieved in source detection and characterization (e.g. completeness, reliability, positional and flux density accuracy). In Section 4 we present the analysis conducted on the resulting source catalogue, from source counts to spectral indices, while in Section 5 we report a comparison with existing astronomical databases and a preliminary study of unclassified sources. Finally, we report in Section 6 a summary of the results obtained and future prospects.

2 OBSERVATIONAL DATA OF THE SCORPIO FIELD

2.1 ASKAP 912 MHz observations and data reduction

The Scorpio field was observed in January 2018 with 15 antennas equipped with the new PAF system version (Mk II) in band 1 (from 792 to 1032 MHz). In this array configuration, the minimum and maximum baselines were respectively 22.4 m and 2.3 km. The former corresponds to a maximum theoretical largest angular scale (LAS) around 50 arcmin at 912 MHz. The total surveyed area covers ∼40 square degrees centred on l=343.5°, b=0.75°, extending by a factor of ∼4.8 the area surveyed with past Scorpio observations done with the Australian Telescope Compact Array (ATCA) (Umana et al. 2015; Ingallinera et al. 2019).

The calibration and imaging procedures adopted to produce the final mosaic (shown in Fig. 1 and referred to as the Scorpio ASKAP map in the rest of the paper) are described in detail in the Scorpio paper 1 (Umana et al. in prep.). The green contour in Fig. 1 delimits the field region considered for source extraction (see Section 3), while the yellow contour denotes the Scorpio region observed with the ATCA telescope at 2.1 GHz (Umana et al. 2015) (see Section 2.2 for details). The synthesized beam of the final map in J2000 coordinates is 24"×21" at a position angle of 89°.

The background level and rms noise were estimated with the CAESAR finder using parameter values reported in Table A1 (available in the online version of this article). The background rms noise was obtained by interpolating the median absolute deviation (MAD) of pixel fluxes computed over moving sampling boxes of size 10 times the area of the synthesized beam. The background level varies considerably across the surveyed area. In Fig. 2 we report the estimated background noise in μJy/beam as a function of the Galactic latitude coordinate b, averaged over the Galactic longitude coordinate l. We observe a noise level ∼200 μJy/beam in regions far from the Galactic plane and without bright sources. Close to the Galactic plane, the background noise increases due to the Galactic diffuse emission and the bright emission from extended sources, filling the beam of the telescopes and increasing the system temperature. In regions free of extended sources we observe a background noise around 500-600 μJy/beam. Only 20% of the field area has a 5σ noise level smaller than 1 mJy/beam, while for ∼70% of the field the 5σ noise is smaller than 2 mJy/beam.

2.2 ATCA 2.1 GHz observations and data reduction

The Scorpio field was observed with the Australia Telescope Compact Array (ATCA) in the 6A and 6D configurations at the reference frequency of 2.1 GHz, using

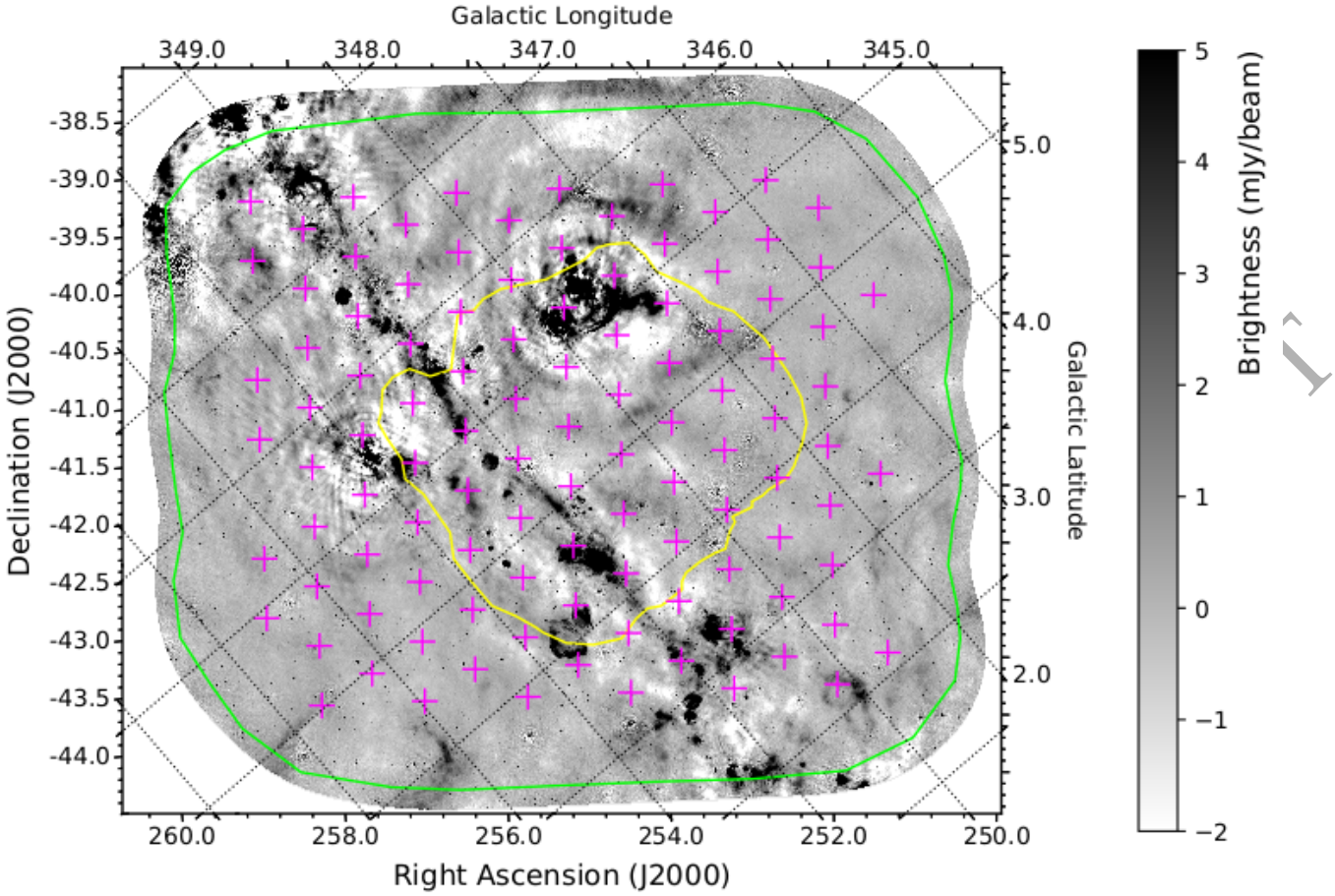

Figure 1. 912 MHz mosaic of the SCORPIO region observed with ASKAP. The purple crosses indicate the beam centre positions for the three interleaved pointings. The green contour delimits the mosaic area considered for source catalogue extraction with the CAESAR source finder. The yellow contour denotes the SCORPIO region observed with the ATCA telescope at 2.1 GHz (see text).

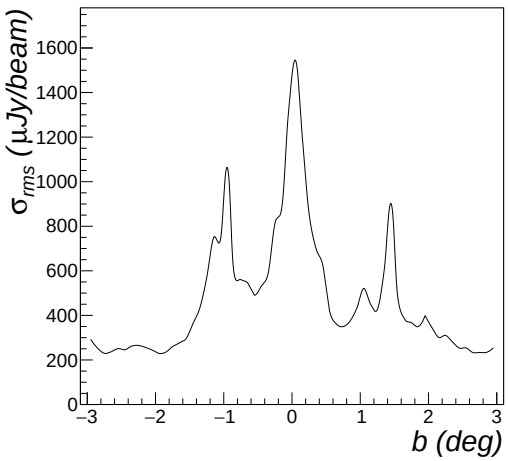

Figure 2. Estimated background noise of SCORPIO mosaic in μJy/beam as a function of the Galactic latitude b and averaged over Galactic longitude l.

the 16-cm CABB receiver (observing band from 1.1 to 3.1 GHz) (Wilson et al. 2011). In this array configuration, the theoretical upper limits for the LAS ranges from ∼4.3 to ∼12.2 arcmin. The observations, conducted in different runs from 2011 to 2012, the data reduction strategy and the scientific results are extensively described elsewhere (Umana et al. 2015; Riggi et al. 2016; Cavallaro et al. 2018; Ingallinera et al. 2019). ATCA observations cover only a small portion of the SCORPIO field observed with ASKAP, equivalent to 8.4 square degrees (see Fig.1 for a comparison of the surveyed area size). In Fig. C1 (available in the online version of this article) we present the SCORPIO ATCA mosaic. We refer to this as the SCORPIO ATCA map. The achieved rms is ∼30-40 μJy/beam and the synthesized beam in J2000 coordinates is 9.8"×5.8" (position angle of -3°).
The ATCA data, obtained with a bandwidth of ∼1.7 GHz, were divided into 7 sub-bands ($\langle\nu$/GHz$\rangle$=1.449, 1.681, 1.844, 2.065, 2.337, 2.614, 2.895) and imaging was independently performed on each of them to produce additional mosaics. The 2.895-GHz channel map was not considered as it was significantly affected by noise and imaging artefacts. The remaining sub-band mosaics (1-6) along with the full band mosaic are used throughout the paper as ancillary data to

complement the ASKAP catalogue with value-added information, such as the source spectral indices (see Section 4.2), or to estimate the expected fraction of extended sources (see Section 4.1).

2.3 MOST 843 MHz observations

The *Molonglo Galactic Plane Survey 2nd Epoch (MGPS-2)* (Murphy et al. 2007), carried out with the Molonglo Observatory Synthesis Telescope (MOST) at a frequency of 843 MHz, completely covers the SCORPIO field observed with ASKAP with a lower spatial resolution (45"×45" cosec$|\delta|$) and a source detection threshold of ∼10 mJy. 799 MGPS sources fall in the SCORPIO region. Their position uncertainty is considered better than 1"-2" (Murphy et al. 2007).

2.4 NVSS 1.4 GHz observations

The *NRAO VLA Sky Survey* (NVSS) (Condon et al. 1998) covers the SCORPIO region north of DEC=-40° at a frequency of 1.4 GHz with an angular resolution of 45". The detection threshold is ∼2.5 mJy. A number of 853 NVSS sources fall in the SCORPIO region.

2.5 TGSS 150 MHz observations

The *TIFR GMRT Sky Survey* (TGSS) (Intema et al. 2017) fully covers the SCORPIO field at the reference frequency of 150 MHz and with an angular resolution of 25"×25"/cos($DEC - 19°$) and a median rms noise of 3.5 mJy/beam. 249 sources from the first alternative data release (ADR) fall in the SCORPIO region.

2.6 GLEAM 200 MHz observations

The *GaLactic and Extragalactic All-sky Murchison Wide-field Array* (GLEAM) survey (Hurley-Walker et al. 2017) partially covers the SCORPIO field in ($1° \leq |b| \leq 10°$, $345° < l < 67°$) at the reference frequency of 200 MHz (bandwidth 60 MHz) with an angular resolution of ∼2 arcmin and an rms noise of 10-20 mJy/beam. 51 sources from the GLEAM Galactic plane catalogue (Hurley-Walker et al. 2019) fall in the SCORPIO region.

2.7 Supplementary surveys

In this work we will also make use of the following infrared surveys for source classification studies (see Section 5.3):

- *AllWISE* (Cutri et al. 2013) of the *Wide-field Infrared Survey Explorer* (WISE, Wright et al. 2010): The survey is fully covering the SCORPIO mosaic region with $\sim 9.3\times10^5$ sources detected with S/N>5 in at least one of the four bands at 3.4 μm (W1), 4.6 μm (W2), 12 μm (W3) and 22 μm (W4). The angular resolutions are 6.1", 6.4", 6.5" and 12" and the 5σ flux sensitivities for point sources are 0.08 mJy, 0.11 mJy, 1 mJy and 6 mJy respectively.
- *GLIMPSE* (Galactic Legacy Infrared MidPlane Survey Extraordinaire) 8.0 μm surveys (Churchwell et al. 2009) of the *Spitzer Space Telescope* (Werner et al. 2004): The surveys (GLIMPSE-I and GLIPMSE-3D) are partially covering (∼74%) the SCORPIO mosaic region with 8.2×10^5 sources detected with S/N>5. The angular resolution is 2" and the 5σ flux sensitivity ∼0.4 mJy.
- *Hi-GAL* (Herschel infrared Galactic plane Survey) 70 μm survey (Molinari et al. 2016) of the *Herschel Space Observatory* (Pilbratt et al. 2010): The survey is partially covering (∼50%) the SCORPIO mosaic region with 5654 sources detected with S/N>5. The angular resolution is ∼8.5" and the 1σ flux sensitivity ∼20 MJy/sr.

3 COMPACT SOURCES IN THE SCORPIO FIELD

3.1 Source finding

Compact sources were extracted from the SCORPIO ASKAP map with the CAESAR source finder (Riggi et al. 2016, 2019) using an iterative flood-fill algorithm in which the detection threshold is initially set to 5σ and the flooding threshold to 2.5σ. At each iteration the background and noise maps are recomputed, excluding the sources found in the previous iteration and the detection threshold is lowered in steps of 0.5σ. Two iterations were used in this work, corresponding to a final 4.5σ seed threshold level. Algorithm parameter values, reported in Table A1 (available in the online version of this article), resulted from a fine-tuning procedure carried out both on the simulated data sample described in Riggi et al. (2019) and on the simulated maps described in Section 3.3.

We detected 5663 islands[1] in the map. 5413 of these were selected as compact source candidates and successfully fitted with a mixture of Gaussian components.

To reject imaging artefacts and sources with a poor quality characterization, we applied these selection criteria to the extracted source sample:

- Source fit converged with a $\tilde{\chi}^2$ <10;
- Positive fitted component peak flux;
- Fitted component centroid inside the source island and the mosaic boundary region;
- Separation between any pair of source components larger than 8" (or 2 pixels)

After the selection, 4262 source islands and 4813 fitted source components are left in the preliminary catalogue.

These source counts still include spurious sources, mainly due to imaging artefacts and over-deblending of extended/diffuse emission, surviving the selection criteria. To produce the final catalogue we visually inspected the entire field labelling each source component as "real" or "spurious" in case of a clear unambiguous identification. 4144 fitted source components were tagged as "real" in the final catalogue. Taking into account that the selected survey region is 37.7 square degrees, a density of ∼110 selected compact sources per square degree is obtained.

In Table 1 we report a summary of the number of sources

[1] By "island" (or "blob") we denote a group of connected pixels with brightness above a merge threshold and around a seed pixel with brightness above a detection threshold. Island counts include also islands nested in other islands.

Table 1. Number of sources extracted from the Scorpio ASKAP mosaic at 912 MHz with the CAESAR finder at different selection stages and per number of fitted components. The NO SEL column reports the number of sources extracted by the source finder without any quality cuts applied. The SEL column reports the number of sources obtained after applying the selection criteria described in the text. The SEL+VIS SEL column reports the number of sources passing both the quality selection and the visual inspection.

# components	Selection		
	NO SEL	SEL	SEL+VIS SEL
0	250	0	0
1	4754	3857	3786
2	440	308	173
3	131	59	4
>3	88	38	0
All	5663	4262	3963

Table 2. Number of sources extracted from the Scorpio ATCA mosaic at 2.1 GHz with the CAESAR finder at different selection stages and per number of fitted components. The NO SEL column reports the number of sources extracted by the source finder without any quality cuts applied. The SEL column reports the number of sources obtained after applying the selection criteria described in the text. The SEL+VIS SEL column reports the number of sources passing both the quality selection and the visual inspection.

# components	Selection		
	NO SEL	SEL	SEL+VIS SEL
0	146	0	0
1	3021	2104	2096
2	465	188	120
3	158	53	11
>3	102	30	0
All	3892	2375	2227

extracted at different selection stages. Source numbers labelled with "SEL+VIS SEL" refer to the number of sources passing both the selection criteria and the visual selection. The number of detected sources classified per number of fitted components is also reported.
Using the same procedure and source selection adopted for the ASKAP catalogue, we extracted 2227 sources and 2369 fitted components from the SCORPIO ATCA mosaics. The source numbers obtained at different selection stages on the full bandwidth map are reported in Table 2.

3.2 Source cross-matching

To validate and complement the ASKAP catalogue, we cross-matched it with the ATCA catalogue and with the catalogues of supplementary radio (MGPS, NVSS, TGSS, GLEAM) and infrared (AllWISE, GLIMPSE, Hi-GAL) surveys listed in Section 2. A summary of the match results is reported in Table 3 and details are provided in the following sections.

3.2.1 Cross-matching with ATCA source catalogue

731 ASKAP source components (out of 856 components in the catalogue falling in the ATCA mosaic region) match with at least one source component from the ATCA catalogue within a search radius of 24". We visually inspected each cross match rejecting spurious and unclear associations, e.g. cases in which the ASKAP source flux density measurement is potentially affected by close background sources visible in the ATCA map but not in ASKAP. We finally selected 648 matches. The majority are one-to-one matches (596), while the remaining (52) are one-to-many matches (up to three components). The number of matches purely arising by chance was estimated by averaging the number of matches found between ASKAP catalogue and multiple random ATCA catalogues in which the measured source positions were uniformly randomized inside the ATCA mosaic. With this procedure we found 3.8±0.3 matches between both catalogues. We thus concluded that ∼99.5 percent of the matches found are likely to be real.

3.2.2 Cross-matching with supplementary radio surveys

We found 688 MGPS sources potentially associated to ASKAP sources within a match radius of 45". 546 of them were finally selected for further analysis after excluding multi-matches and sources with potentially unreliable flux densities, e.g. affected by imaging artefacts or closely located to very extended sources.
Within a match radius of 45" we found 226 NVSS sources matching to one or more ASKAP source components. 189 single matches were finally selected after a visual inspection. 192 out of 217 TGSS source matches can be associated to a single ASKAP source within a match radius of 24". Similarly, 32 out of 40 GLEAM source matches found within a radius of 45" were selected for further analysis after excluding multi-matches or ambiguous associations.

3.2.3 Cross-matching with supplementary infrared surveys

For the cross-match we considered the AllWISE survey as the primary dataset reference due to its full coverage. To limit the number of spurious associations, we selected sources with S/N>5 in both the W3 and W4 bands with a fraction of saturated pixels smaller than 10%, reducing the number of sources within the ASKAP field to $\sim 1.2\times10^5$. A crossmatch with ASKAP source catalogue using a match radius equal to the ASKAP beam size (24") yields 1319 matches. About 2900 catalogued sources do not therefore have IR counterparts with fluxes above W3 and W4 detection thresholds. The number of source associations arising by chance, estimated using artificial catalogues with random offsets applied, is however compatible with the number of obtained matches, indicating that the vast majority of the matches are spurious.
Selecting a smaller radius (e.g. 8" as in the Galactic object search analysis) and requiring flux information in all bands, leads to 384 associations allowing us to reduce the number of potential spurious matches to ∼40%. The number of associations decreases to 225 and 41, respectively if we require triple and quadruple matches with GLIMPSE and Hi-GAL catalogues.

Table 3. Number of cross-matches found between ASKAP source component catalogue and different radio and infrared surveys. Column 4 reports the total number of sources falling in the SCORPIO mosaic for each survey catalogue. In the last two rows we summed up the number of sources from different catalogues.

Surveys	radius (")	#matches	total
ATCA	24	648	2369
MGPS	45	546	799
NVSS	45	189	853
TGSS	24	192	249
GLEAM	45	32	51
AllWISE	8	384	123374
AllWISE + GLIMPSE	8	225	-*
AllWISE + GLIMPSE + Hi-GAL	8	41	-†

* GLIMPSE catalogue has 820112 sources in SCORPIO
† Hi-GAL catalogue has 5654 sources in SCORPIO

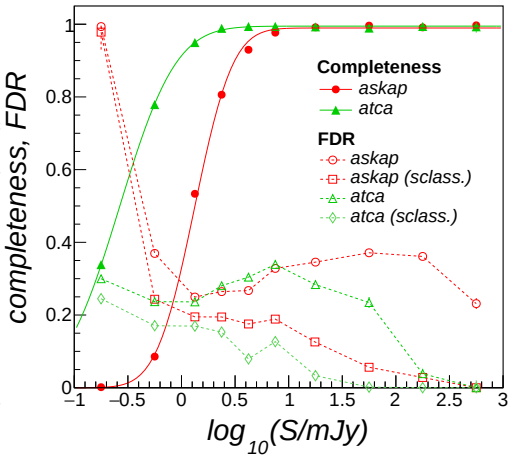

Figure 3. Completeness (filled markers) and false detection rate (FDR) (open markers) as a function of the injected and measured source flux density respectively obtained on the simulated ASKAP (red markers) and ATCA (green markers) source catalogues. Solid lines represent the fitted completeness model of equation 1. Open squares and diamonds (labelled as "sclass") represent the false detection rate obtained after applying a neural network classifier, trained to identify spurious fit components in the catalogue.

The impact of the 5σ limits requested in W3 and W4 bands was investigated on the star/galaxy/quasar dataset provided by Clarke et al. (2020)[2]. The magnitude selection cuts W3<11.32 and $W4<8.0$[3] were found to remove a very large fraction (∼98%) of extragalactic sources from the sample but, unfortunately, also potential radio stars. We thus expect the unmatched sources to be mostly extragalactic, with a smaller percentage of "IR-quiet" (e.g. pulsars) or faint mid-infrared Galactic objects.

3.3 Catalogue selection effects and uncertainties

To evaluate the expected source extraction and characterization accuracy of the produced catalogue, we made use of both simulated data and cross-matches found with other surveys.
Simulated samples were drawn from the SCORPIO mosaics (both ASKAP and ATCA) using the following approach[4]. First, a residual map was obtained by subtracting all compact sources down to a very low detection threshold (2σ). Imaging artefacts, extended and diffuse sources were not removed. A sample of 50 simulated maps was then generated by artificially adding uniformly spaced point sources to the residual mosaic, with a density of 100 deg^{-2} and exponential flux density distribution ($\propto e^{-\lambda S}$ with λ=1.6, as for real data above the detection threshold). CAESAR was finally run on the simulated maps and the same set of quality criteria used for the SCORPIO mosaics were applied to the simulated catalogue. Source extraction and characterization metrics were estimated by cross-matching injected sources with extracted sources.

3.3.1 *Completeness and reliability*

Catalogue completeness and reliability were studied with simulated data as a function of the source flux density.

Sources injected in the simulated maps are considered as the true catalogue. Extracted sources that do not crossmatch to any injected source are thus counted as false detections and contribute to increase the false detection rate (or decrease the reliability). Results are reported in Fig. 3 for both ASKAP (red markers) and ATCA (green markers) simulated data. The completeness C is shown with filled markers and can be parametrized as a function of the flux density S as:

$$C = \frac{C_0}{2}\left(1+\mathrm{erf}\left\{\frac{\log_{10}(S)-\log_{10}(S_0)}{k}\right\}\right) \quad (1)$$

with parameters: C_0=0.99, $\log_{10}(S_0)$=−2.88, k=0.40 (ASKAP) and C_0=0.99, $\log_{10}(S_0)$=−3.58, k=0.59 (ATCA). For ASKAP (ATCA) observations we expect the catalogue to be >90% complete above 5 mJy (1 mJy).
The false detection rate, reported in Fig. 3 with open dots (ASKAP) and open triangles (ATCA), is found to be of the order of 20-30%, slightly decreasing by a few percent when moving away from the Galactic plane. False detections are largely due to sidelobes around bright sources (compact or extended) and overdeblending of extended sources. Reliability can be improved by ∼10% after applying a neural network classifier previously trained to identify "good" sources from the data (see Riggi et al. 2019 for more details). Results are shown in Fig. 3 with open squares (ASKAP) and open diamonds (ATCA). To further reduce the false detection rate to acceptable levels (below 1%) we visually inspected the produced catalogue removing spurious sources that were not identified in the automated procedure (see Section 3.1).
For the future we expect this can be substantially improved in multiple ways, e.g. increasing the number of classifier parameters, tuning of classifier hyperparameters, introducing specialized classifiers trained to identify imaging artefacts

[2] 10.5281/zenodo.3768398
[3] See the WISE Explanatory Supplement at http://wise2.ipac.caltech.edu/docs/release/allsky/expsup/
[4] Simulation tasks (compact source subtraction, point-source generation) can be performed using application scripts provided along with CAESAR.

(e.g. around bright sources) which cannot be efficiently removed with the classifier adopted in this work.

3.3.2 Source position accuracy

Positional uncertainties in RA and Dec can be expressed as:

$$\sigma_\alpha = \sqrt{\sigma^2_{\alpha,fit} + \sigma^2_{\alpha,cal}}$$
$$\sigma_\delta = \sqrt{\sigma^2_{\delta,fit} + \sigma^2_{\delta,cal}} \quad (2)$$

where σ_{fit} are the position uncertainties due to the fitting process (including noise and uncertainties in fit parameters) while σ_{cal} are the uncertainties due to the calibration process.

σ_{fit} is provided by the fitting routine for each source and can be compared with values obtained from simulated data as a function of the source signal-to-noise ratio (S/N). We found that the fit uncertainties are largely underestimated with respect to the expected values found in the simulations. The latter are a factor 3-4 larger than the semi-analytical estimates provided by Condon (1997)[5]. This is partly expected given that the semi-analytical estimate and the estimate obtained from the fitting routine are neglecting the effect of the correlated noise in the map. A correction for this effect, for example using equation 41 of Condon (1997) in the maximal-smoothing limit, would yield an expected analytical uncertainty ∼2.6 larger. We have finally set σ_{fit} to the values obtained from the simulations and parametrized it as a function of S/N as:

$$\sigma^{\rm ASKAP}_{\alpha,fit} = \frac{9.86}{S/N}\ \text{arcsec}, \quad \sigma^{\rm ASKAP}_{\delta,fit} = \frac{6.01}{S/N}\ \text{arcsec}$$
$$\sigma^{\rm ATCA}_{\alpha,fit} = \frac{2.28}{S/N}\ \text{arcsec}, \quad \sigma^{\rm ATCA}_{\delta,fit} = \frac{2.98}{S/N}\ \text{arcsec} \quad (3)$$

Position fit uncertainties are of the order of 1.5”-1.8” (0.5”-0.6”) at the detection threshold and better than 0.5” (0.15”) with S/N>20 for ASKAP (ATCA) data.

Calibration uncertainties σ_{cal} can be inferred from the position spread observed in bright sources with respect to a reference catalogue. The Radio Fundamental Catalogue (RFC, version rfc_2020b)[6], for instance, contains ∼17000 radio sources measured in multiple VLBI observations with milliarcsecond accuracy. 5 RFC sources, detected in the X band, cross-match with ASKAP bright sources (four with $S/N > 200$ and one with $S/N > 20$) and have position uncertainty smaller than 0.02”. The standard deviations (s_α=0.5”, s_δ=0.4”) of the observed position offset provide a first measure of σ_{cal} since both RFC and ASKAP fit position uncertainties are negligible at high S/N. Additionally, we inferred ASKAP calibration errors using 344 and 80 sources with S/N>50 matching to MGPS and NVSS catalogues, respectively. The observed standard deviations (s_α=1.3”-1.5”, s_δ=1.3”-1.4”) suggest a slightly larger calibration uncertainty of $\sigma_{cal,\alpha}$=1.0”-1.1” and $\sigma_{cal,\delta}$=0.8”-1.1”, after subtracting (in quadrature) the ASKAP fit errors and the MGPS (∼0.9” from Murphy et al. 2007) or NVSS (∼1” from Condon et al. 1998) uncertainties.

As no ATCA-RFC matches were found, to infer calibration errors for ATCA, we considered 38 sources detected with S/N>50 and matched to MGPS sources. In this case, we did not use NVSS data as no matches were found with ATCA above the considered significance level. From the offset standard deviations (s_α=2.1”, s_δ=2.5”), we obtained a calibration uncertainty of $\sigma_{cal,\alpha}$=1.9” and $\sigma_{cal,\delta}$=2.4”, after subtracting (in quadrature) the ATCA fit errors and the MGPS uncertainties. Such estimates should be regarded as upper limits if MGPS positional uncertainties are underestimated.

Systematic offsets possibly introduced by the fitting procedure were investigated with simulated data for both ASKAP and ATCA. No bias (e.g. median offsets smaller than 0.04”) was found and, hence, no corrections were applied to the catalogues.

To assess the absolute positional accuracy of the ASKAP ESP data, we considered the median offsets found with respect to the matched sources in RFC, ATCA, MGPS and NVSS catalogues. We considered only the ASKAP sources with S/N>50. From the comparison, we found that the ASKAP Dec offsets are negligible (smaller than 0.05”), while the ASKAP RA is systematically higher than that of the reference catalogues: $\langle\alpha\rangle$=1.4” (RFC), $\langle\alpha\rangle$=1.4” (ATCA), $\langle\alpha\rangle$=1.6” (NVSS), $\langle\alpha\rangle$=1.7” (MGPS)[7]. The RA offset is consistent as a function of the ASKAP source flux density above S/N>20 (e.g. varying by ∼0.2 at most from bin to bin) and slightly larger than the total position uncertainties estimated above. The astrometric offset, affecting also other ASKAP Early Science observations, is due to a known bug in the ASKAPSoft software version used to process SCORPIO ASKAP15 data. Recent analysis carried out on newer observations done with the full ASKAP array and improved versions of the reduction software and calibration procedure, do not report significant astrometric offsets. Indeed, we were not able to detect comparable offsets from the preliminary SCORPIO ASKAP36 maps. For this analysis, we have decided to account for the observed systematic offset by increasing the calibration uncertainty to 1.5”.

3.3.3 Source flux density accuracy

Uncertainties on the measured flux density S are mainly due to the uncertainties of the source fitting process in the presence of noise (σ_{fit}, expressed here as a percentage of the flux density) and the flux scale calibration uncertainties (σ_{cal}, usually given as a percentage of the flux density). Total relative uncertainties σ can be therefore expressed as:

$$\sigma = \sqrt{\sigma^2_{fit} + \sigma^2_{cal}} \quad (4)$$

σ_{fit} values for each source are obtained by error propagation using source parameter errors provided by the fitting routine. These were found a factor ∼3 smaller with respect to the expected values obtained from simulated data. Similarly to what was done in Section 3.3.2, we have set the fit

[5] A discrepancy (a factor ∼2) between analytical and measured uncertainties was observed also in other analysis carried out with simulated data using CAESAR (Riggi et al. 2019) or alternative finders (Hopkins et al. 2015).

[6] http://astrogeo.org/rfc/

[7] The median offset was found to be 2.7” but we corrected for the systematic offset of -1” reported in Murphy et al. 2007 with respect to NVSS data.

uncertainties for both ASKAP and ATCA data to the following parametrized values, derived from the simulations as a function of the source signal-to-noise ratio (S/N):

$$\sigma_{fit}^{ASKAP} = 0.14 \times [\log_{10}(S/N)]^{-2.72}$$
$$\sigma_{fit}^{ATCA} = 0.14 \times [\log_{10}(S/N)]^{-2.74} \quad (5)$$

Fit uncertainties are ∼35% at the detection threshold and better than 5% with S/N>30.

It is now known from simulation studies (Hopkins et al. 2015; Riggi et al. 2019) that many source finders produce a biased flux density measurement as they approach the detection threshold. CAESAR, like other widely used finders (e.g. SELAVY, AEGEAN, PYBDSM), tends to overestimate the flux density at low S/N. As discussed in Hopkins et al. (2015), this is likely due to a poorly constrained Gaussian fit. Systematic flux density offsets $\langle \Delta S/S \rangle_{fit}$ were therefore characterized using simulated data and parametrized as a function of the source S/N as follows:

$$\langle \Delta S/S \rangle_{fit}^{ASKAP} = 0.05 \times [\log_{10}(S/N)]^{-4.97}$$
$$\langle \Delta S/S \rangle_{fit}^{ATCA} = 0.06 \times [\log_{10}(S/N)]^{-4.22} \quad (6)$$

Systematic fit biases are ∼25-30% at the detection threshold and smaller than ∼1% with S/N>25. Measured flux densities in both ASKAP and ATCA catalogues were corrected using the above parametrizations.

To assess the absolute flux density scale reliability, we carried out a comparison of the measured ASKAP source flux densities with those reported in previous catalogues at a nearby frequency, such as the MGPS source catalogue. The correlation between ASKAP (S_{912}) and MGPS (S_{843}) source flux densities is reported in the top panel of Fig. 4. The dashed black line corresponds to a perfect correlation (S_{912}=S_{843}). The bottom panel represents the median relative flux density difference observed as a function of the MGPS flux density. Error bars correspond to the semi-interquartile range of the data in each bin. If all sources were to have a single power-law spectrum $S \propto \nu^{\alpha}$, we would ideally expect to observe a relative difference of $(912/843)^{\alpha}-1$ between the two catalogues. Expected offsets are shown in Fig. 4 with black dashed and dotted lines for three choices of expected spectral indices: α=−0.7 for extragalactic sources, α=0 for Galactic sources with thermal-dominated emission and an average α=−0.9 as observed in Section 4.2 or in other radio surveys in the Galactic plane (Cavallaro et al. 2018; Wang et al. 2018). For sources brighter than ∼70 mJy, less affected by possible flux density reconstruction bias on both catalogues, we observe that ASKAP flux densities are on average larger by ∼3% with respect to MGPS fluxes. Provided that the source sample is not completely dominated by Galactic thermal sources, we would infer that ASKAP fluxes are overestimated by 9-10% compared to those expected from a mixed population of sources with an average spectral index of −0.9.

We also compared the ASKAP flux densities of selected sources with those expected from a power-law fit obtained with at least four spectral points using MGPS, NVSS and ATCA data. 45 sources (28 with S/N>50) are well-modelled by a power-law ($\tilde{\chi}^2$<2, spectral indices ranging from −0.7 to −0.9) over the entire frequency range and, thus, can be used as additional flux calibrators. ASKAP flux densities for these sources were on average found in excess by

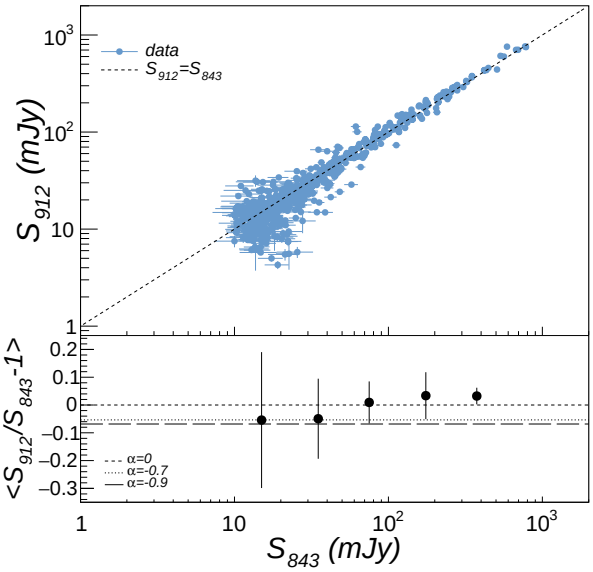

Figure 4. Top: Correlation between flux densities S_{912} and S_{843} of cross-matched sources found in ASKAP (912 MHz) and MGPS (843 MHz) catalogues. The dashed black line corresponds to a one-to-one relation (S_{912}=S_{843}). Bottom: Relative difference between ASKAP and MGPS flux densities. Black dashed and dotted lines represent the difference expected from $S \propto \nu^{\alpha}$ for three different spectral indices (0,-0.7,-0.9).

∼10% (S/N<50) and ∼5% (S/N>50) with respect to the predicted values. The standard deviation of the observed offset of bright sources (S/N>50) is ∼5% and can be used as a measure of σ_{cal}. These results suggest a flux density scale inconsistency in the ASKAP data calibration or imaging process that has to be investigated with the full array and improved releases of the data reduction pipeline. The origin of the observed shift is in fact not fully understood at this early stage stage of ASKAP observations in which the calibration process is not yet optimized. For this reason, we have decided not to correct for it and assume a larger calibration uncertainty (10%) to carry out the analysis described in Section 4. For the ATCA data we have instead assumed σ_{cal}=3% following previous works on the SCORPIO field (Cavallaro et al. 2018).

4 ANALYSIS

4.1 Estimation of the fraction of resolved sources

A widely used method (Franzen et al. 2015, 2019) to identify non point-like sources in the catalogue is based on the ratio S/S_{peak} between the integrated and peak flux density which is expected to be larger than 1 for extended sources. In the XXL survey by Butler et al. (2018), sources were classified as resolved if they fulfil the following empirical relation:

$$S/S_{peak} > a + \frac{b}{S/N} \quad (7)$$

with a =1.08 to account for possible calibration errors and b=2.03, defined so as to keep 90% of the data having S/S_{peak}<1 above the curve S/S_{peak}= a - $\frac{b}{S/N}$. We tuned the

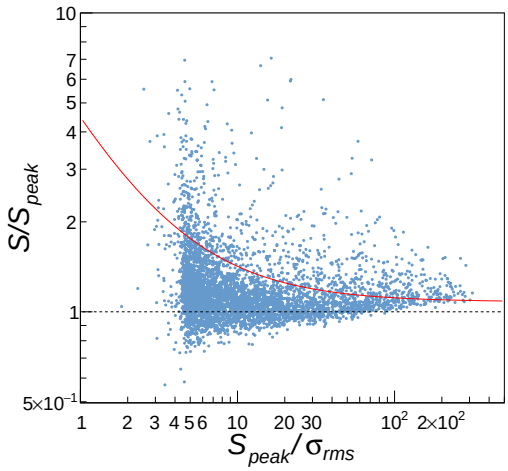

(a) Integrated to peak ratio vs S/N

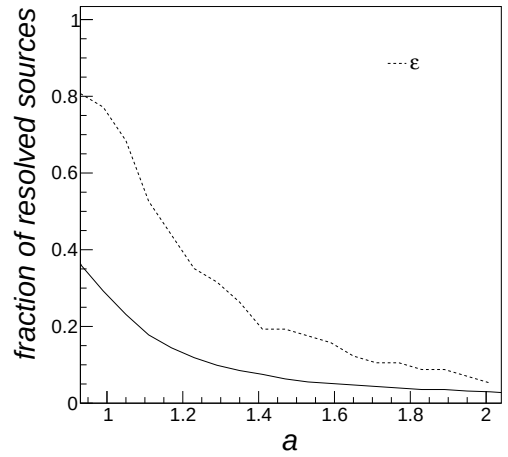

(b) Resolved source fraction

Figure 5. Upper panel: Ratio between integrated S and peak S_{peak} flux densities for catalogued sources as a function of their signal to noise ratio S/N. The red line indicates the curve $S/S_{peak}=a+\frac{b}{S/N}$ (a=1.08, b=3.4), used in the XXL survey, above which sources are labelled as resolved. Lower panel: Fraction of catalogued sources that would be classified as resolved as a function of the applied threshold on the parameter a (with b fixed to 3.4), shown with a solid black line. The dashed black line represents the fraction of truly resolved sources ε (found by comparison with ATCA data) that would be classified as resolved as a function of the applied threshold on the parameter a.

value of b for ASKAP Scorpio survey using simulated data (see Section 3.3). To have less than 5% of misclassified simulated point-sources, the value of b has to be increased to ∼3.4. In Fig. 5(a) we report the S/S_{peak} as a function of S/N for Scorpio source components. The red line represents the empirical function used in the XXL survey with parameters: a=1.08, b=3.4. We report in Fig. 5(b) the fraction of catalogued sources that would be classified as extended if thresholded in S/S_{peak} as a function of the applied threshold on the parameter a (solid black line), assuming b fixed to 3.4. Adopting the same criterion as in the XXL survey (a=1.08) we would classify ∼20% of the catalogued sources as resolved. This is comparable to values reported in other surveys carried out in the Galactic plane (e.g. ∼20% in the THOR survey (Wang et al. 2018)) or far from the Galactic plane and with different spatial resolutions (e.g. see Butler et al. 2018 and references therein)[8].

Table 4. Number of ASKAP sources detected at one or multiple radio frequencies after cross-matching them with MGPS, ATCA (also including sub-band data) and NVSS catalogues.

# frequencies	# sources	percentage(%)
1	2986	72.1
2	504	12.2
>2	654	15.8
3	119	2.9
4	25	0.6
5	52	1.3
6	63	1.5
7	222	5.4
8	152	3.7
9	21	0.5

Using the Scorpio ATCA higher resolution image, it is possible to estimate the number of truly resolved sources at least for a portion of the Scorpio field. In Section 3.2.1 we found that 52/648 ASKAP sources match to more than one ATCA source, e.g. ∼8% of the ASKAP catalogued sources have a genuine extended nature. Using this limited source sample, we can compute the fraction of truly resolved sources that would be classified as extended, ε, according to the S/S_{peak} criterion described above. We report the results in Fig. 5(b) with a dashed black line. As can be seen, the S/S_{peak} parameter is not sensitive enough to allow a perfect identification of known resolved sources (e.g. for a=1.08 we obtained an identification efficiency of ∼60%).

We therefore repeated the analysis including additional parameters. Following Riggi et al. (2019), we considered in particular the ratio E/E_{beam} between the source fitted ellipse eccentricity E and the beam ellipse eccentricity E_{beam}. We found no significant improvements in the extended source identification capabilities compared to the case of a single discriminant parameter. In light of these results, we will conservatively assume ∼8% as a lower limit in the fraction of extended sources expected in the reported catalogue. Future observations of the Scorpio field with the complete array and at higher ASKAP frequencies will provide an improved angular resolution (by a factor of 3-4), enabling a direct identification of additional extended sources over the entire field.

4.2 Spectral indices

Following the convention $S \propto \nu^{\alpha}$ (where S is the integrated source flux), we estimated the spectral index α of ASKAP catalogued sources using the cross-matches found in Section 3.2 with the ATCA (including also sub-band data), MGPS and NVSS source catalogues. The number of ASKAP

[8] For comparison, the angular resolution of XXL and THOR survey are 4.8" and 25", respectively.

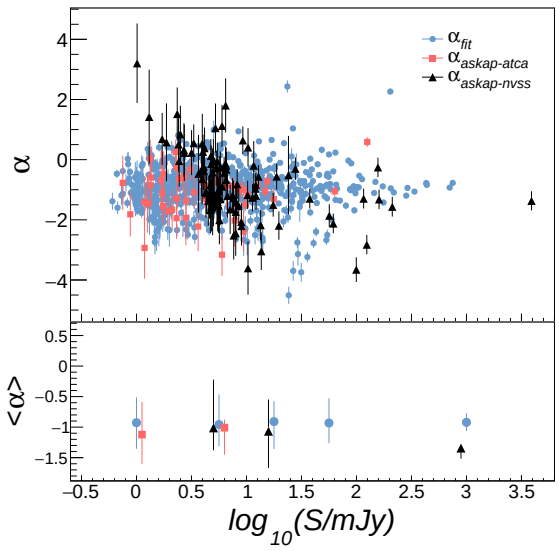

Figure 6. Top panel: Spectral indices of ASKAP 912 MHz source components as a function of ASKAP flux density. Blue dots represent the spectral indices obtained from a power-law fit of available ASKAP-ATCA-NVSS-MGPS data, while the red squares and black triangles indicate the spectral indices obtained from only ASKAP-ATCA and ASKAP-NVSS frequencies, respectively. Bottom panel: Median spectral index for the three samples as a function of ASKAP flux density. Error bars are the interquartile range (IQR) in each flux density bin.

sources detected at one or multiple radio frequencies are reported in Table 4. More than 70% of the sources do not cross-match with any of the considered catalogues and thus no spectral index information can be reported for them. 12% of the sources have flux information only at two frequencies. For them only a two-point spectral index can be reported. These are to be considered as first-order estimates and might not represent a good estimate particularly for sources in which a turnover is present between the two frequencies. For example this is the case for some of the Gigahertz Peaked Spectrum (GPS) and Compact Steep Spectrum (CSS) radio sources (about 40, or ∼20%, in the compilation presented in Jeyakumar 2016). For spectral indices obtained only from ASKAP and ATCA data, taking into account the source extraction performance in both catalogues, we expect to obtain an unbiased estimate of α above 10 mJy at 912 MHz with uncertainties smaller than ∼0.2.

For ∼16% of the sources, we have flux information in at least three different frequencies. These data were fitted with a power-law model to determine the spectral indices. When the fit does not converge or does not pass a minimum quality criterion ($\tilde{\chi}^2$<10), e.g. due to the presence of outliers in one or more frequency bands, a robust linear regression is performed excluding data points with larger fit residuals. Without improvement (e.g. the $\tilde{\chi}^2$ of the robust fit is still larger than the quality threshold), the reported source spectral index is finally set to the value found using only two frequencies, ASKAP-ATCA or ASKAP-NVSS (if no ATCA information is available).

In Fig. 6 (upper panel) we report the spectral indices obtained from the radio spectrum fitting procedure (635 sources, blue dots) on available ASKAP-ATCA-NVSS-MGPS matches, and those obtained using only ASKAP-ATCA (49 sources, red squares) and ASKAP-NVSS (96, black triangles) matches. Some sources (∼1% of the sample) have a rather extreme spectral index (α<−3 or α>2.5). Although there is a chance they are pulsars (α<−3) or hyper-/ultra-compact HII regions with an optically thick free-free emission (α>2.5), their measured indices are somewhat questionable. We note that the majority of the potentially unreliable indices are indeed obtained from two nearby frequencies (ASKAP-NVSS), for which a change in flux density (e.g. due to errors) of ∼10% would lead to a ∼0.5 variation in the measured spectral index. These spectral indices should therefore be treated with caution and be re-estimated with data at additional frequencies. Five sources, in particular, present a very steep spectrum (α<−3), obtained by fitting ASKAP, MGPS and NVSS data. Spectral index values are in this case mainly determined by NVSS measurements. From a visual inspection we were not able to spot possible issues in the ASKAP or MGPS flux estimate, e.g. due to a complex background or imaging artefacts. NVSS data for two sources (J171435−392543, J171448−394756) are instead considerably affected by artefacts and thus the reported flux densities may be not accurate. Future ASKAP SCORPIO observations, bridging the frequency gap between MGPS and NVSS measurements, will allow us to determine the spectral slope more reliably.

Median spectral indices are reported in the bottom panel of Fig. 6 as a function of the ASKAP source flux density. The median value of fitted spectral indices for brighter sources (>10 mJy) is $\langle\alpha\rangle = -0.92$ (IQR=0.68). A robust least squares linear fit to the data of Fig. 6 (top panel) yields similar values. These estimates are consistent within the quoted uncertainties with those obtained in a completely independent analysis (Cavallaro et al. 2018) carried out on a portion of the SCORPIO ATCA field using only ATCA sub-band data.

4.3 Source counts

In Fig. 7(b) (filled black dots) we report the differential source counts dN/dS (number of sources N per unit area per unit flux density S) obtained by dividing the number of sources found in each flux density bin by the survey area (37.7 deg^2 ∼11.5×10^{-3} sr) and flux density bin width. Counts were not corrected for expected source detection efficiency and flux density reconstruction accuracy (bias and uncertainty) and were normalized by $S^{-2.5}$ (the Euclidean slope) (Condon 1984) as conventionally done in other studies of source counts. Error bars denote the statistical Poissonian uncertainties on the obtained counts.

To compare it with other surveys we need to unfold the source detection effects from the measured counts. The former have been modeled through a response matrix $\mathbf{R} = [r_{ji}]$ expressing the probability for a source with true flux density $x \equiv \log_{10}(S_{true})$ in bin i to be detected with measured flux density $y \equiv \log_{10}(S_{meas})$ in bin j. r_{ji} is computed for each flux density bin (i,j) as:

$$r_{ji} = \int_{y_j-\Delta y_j/2}^{y_j+\Delta y_j/2} \int_{x_i-\Delta x_i/2}^{x_i+\Delta x_i/2} \frac{\varepsilon(x)\varepsilon^{reso}(x)}{\sqrt{2\pi}\sigma(x)} \exp\left\{-\frac{(y-x)^2}{2\sigma^2(x)}\right\} dx\, dy$$

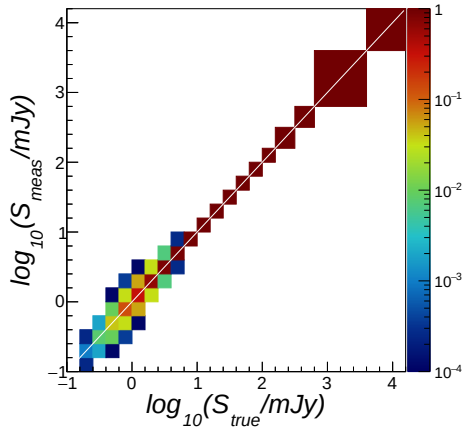

(a) Response matrix

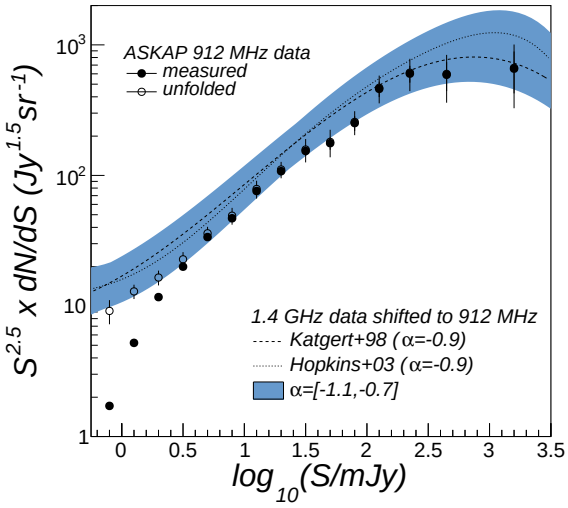

(b) Differential source counts

Figure 7. Top: Response matrix used to unfold source detection effects (detection efficiency, flux bias and uncertainty) from raw source counts. The color represents the probability r_{ji} for a source with true flux density in bin i to be detected with measured flux density in bin j; Bottom: Differential uncorrected source counts of the SCORPIO survey catalogue normalized to standard Euclidean counts ($\propto S^{-2.5}$) shown with filled black dots. Open black dots represents the unfolded differential source counts obtained with the procedure described in the text and using the response matrix above. The shaded area represents the existing extragalactic source count data at 1.4 GHz, parametrized by Katgert (1988); Hopkins et al. (2003) and shifted to a frequency of 912 MHz assuming a spectral index α ranging from −1.1 to −0.7 (central value −0.9). Values relative to the median spectral index −0.9 are shown as dashed and dotted lines, respectively.

(8)

where x_i, Δx_i and y_j, Δy_j are the true and measured flux density bin centres and widths. σ and ε are the flux density uncertainty and the source detection efficiency, respectively[9]. Both have been parametrized as a function of the true flux density using simulated data (see Sections 3.3.3 and 3.3.1). ε^{reso} is introduced to correct for the catalogue incompleteness effect related to the source angular size and known as the "resolution bias". Resolved sources with the same integrated flux density of point sources have in fact lower peak flux densities and thus a higher chance to be missed in the catalogue as falling below the source detection threshold. The response matrix was finally normalized such that the probabilities for a true flux density bin i sum up to the overall efficiency in bin i, e.g. $\varepsilon_i \varepsilon_i^{reso}$.

ε^{reso} was set equal to $1 - h(> \phi_{lim})$, where $h(> \phi_{lim})$ is the fraction of sources above a maximum angular size ϕ_{lim} being missed as resolved. $h(> \phi_{lim})$ was estimated as a function of the flux density as described in Windhorst et al. (1990); Prandoni et al. (2001); Thorat et al. (2013); Retana-Montenegro et al. (2018):

$$\varepsilon^{reso} = 1 - h(> \phi_{lim}) \tag{9}$$

$$h(> \phi_{lim}) = \exp[-\ln 2(\phi_{lim}/\phi_{median})^{0.62}] \tag{10}$$

$$\phi_{median} = \begin{cases} 2" & S_{1.4\,\mathrm{GHz}} \leq 1\,\mathrm{mJy} \\ 2" \times S_{1.4\,\mathrm{GHz}}^{0.3} & S_{1.4\,\mathrm{GHz}} > 1\,\mathrm{mJy} \end{cases} \tag{11}$$

$$\phi_{lim} = max(\phi_1, \phi_2) \tag{12}$$

$$\phi_1 = \sqrt{b_{maj} b_{min} \times (S/S_{thr} - 1)} \tag{13}$$

$$\phi_2 = \sqrt{b_{maj} b_{min} \times (a + \frac{b}{S/\sigma_{rms}})} \tag{14}$$

where b_{maj}=24" and b_{min}=21" are the beam sizes, σ_{rms}=300 μJy/beam is the minimum noise value in the map, S_{thr}=1.5 mJy is the source minimum detection threshold[10], $S_{1.4\,\mathrm{GHz}}$ is the integrated flux density at 1.4 GHz computed using a spectral index of α=−0.9 according to the results obtained in Section 4.2 and in Cavallaro et al. (2018). a=1.08 and b=2.03 are the parameters used in Section 4.1 for the identification of resolved sources.

The resulting matrix values are reported in Fig. 7(a). Above 5 mJy, the correction applied to the source counts is negligible as the catalogue is >98% complete, as shown in Fig. 3, and the flux uncertainty is typically below 1%. Below 5 mJy, the flux uncertainty rapidly increases (up to 30% at 1 mJy) while the completeness rapidly degrades to zero. Source detection inefficiency, thus, causes true counts to be underestimated by a factor ε, while finite flux density uncertainty cause sources to migrate from true to measured flux density bins. As a result, the observed counts in a given bin is contaminated by upward fluctuations from the adjacent lower bins and downward fluctuations from the adjacent upper bins. If the true source counts is steeply falling with flux density, fluctuations from the lower bins dominate and the net effect is an overestimation of the counts.

Resolution bias also causes an underestimation of the true counts. Computed correction factors were found of the order of 5% at 5 mJy and smaller than 1% above 50 mJy.

To derive the corrected counts $\boldsymbol{\mu}$ from uncorrected counts

[9] No bias term is included in equation 8, as we already corrected our data for measurement bias.

[10] The minimum detection threshold value corresponds here to the 5σ threshold with respect to the minimum noise (σ_{rms}=300 μJy/beam) in the map, not to the "effective" detection threshold, averaged over the mosaic, which amounts to ∼5 mJy.

$\boldsymbol{\nu}$, knowing the response matrix $\mathbf{R}$, we need to solve the following system of equations:

$$\underbrace{\begin{pmatrix} \nu_1 \\ \vdots \\ \nu_M \end{pmatrix}}_{\boldsymbol{\nu}} = \underbrace{\begin{pmatrix} r_{11} & r_{12} \cdots & r_{1N} \\ \vdots & \vdots & \ddots \\ r_{M1} & r_{M2} \cdots & r_{MN} \end{pmatrix}}_{\mathbf{R}} \times \underbrace{\begin{pmatrix} \mu_1 \\ \vdots \\ \mu_N \end{pmatrix}}_{\boldsymbol{\mu}} \quad M \geq N \tag{15}$$

where M is the number of flux bins for the uncorrected counts and N is the number of flux bins for the corrected counts. To determine the corrected counts $\widehat{\boldsymbol{\mu}}$ we made use of a forward-folding procedure. First we considered a model $f(\log_{10} S_{true}; \Theta)$ with parameters Θ describing the true source counts $\boldsymbol{\mu}_{model}$ as a function of $\log_{10} S_{true}$. The model folded with the response matrix $\mathbf{R}$ was fitted to the observed counts $\boldsymbol{\nu}$ using a maximum likelihood approach. The best fit provides the expected true model counts $\widehat{\boldsymbol{\mu}}_{model}$ and the corresponding observed model counts $\widehat{\boldsymbol{\nu}}_{model}$. Corrected counts are finally computed as:

$$\widehat{\boldsymbol{\mu}} = \boldsymbol{\nu} * \frac{\widehat{\boldsymbol{\mu}}_{model}}{\widehat{\boldsymbol{\nu}}_{model}} \tag{16}$$

We modeled the true source counts with a power-law functional form. This was found to provide a good fit (χ^2/ndf=44.5/45) to our source flux density data above the detection threshold.

The unfolded differential source counts, normalized by $S^{-2.5}$, are reported in Fig. 7(b) with open black dots while numerical values are reported in Table 5. The error bars represent the total uncertainties $\sigma_{\rm tot}=\sqrt{\sigma^2_{\rm stat}+\sigma^2_{\rm syst}}$ on the unfolded counts, where $\sigma_{\rm stat}$ are the statistical uncertainties, obtained from the Poissonian errors on the uncorrected counts, and $\sigma_{\rm syst}=\sqrt{\sigma^2_{\rm fit}+\sigma^2_{\rm matrix}+\sigma^2_{\rm cal}}$ are the systematic uncertainties. $\sigma_{\rm fit}$ and $\sigma_{\rm matrix}$ are obtained by propagating the likelihood fit parameter errors and the response matrix uncertainties in the unfolded counts, respectively. Matrix uncertainties have been computed by taking the variance of several response matrices randomized around parametrization errors for ε and σ. Additionally, following Windhorst et al. (1990), a 10% uncertainty is considered in the resolution bias correction ε_{reso}. To estimate $\sigma_{\rm cal}$, we shifted the measured flux densities by ±10% (the calibration uncertainty quoted in Section 3.3.3), repeated the unfolding procedure on the resulting "shifted" spectra and compared the obtained counts with "unshifted" counts.

Existing source count data at 1.4 GHz, as parametrized by Katgert (1988); Hopkins et al. (2003) and shifted to a frequency of 912 MHz (assuming a spectral index α ranging from −1.1 to −0.7), are shown for comparison as a shaded blue area. The shaded area also accounts for the count fluctuations (∼20%) reported in past works comparing source counts from different extragalactic fields (Windhorst et al. 1990; Hopkins et al. 2003) or from different regions of the same survey (Prandoni et al. 2001; Retana-Montenegro et al. 2018). The observed spread can be due to either systematic uncertainties, different correction factors applied, or to the large scale structure of the universe (i.e. cosmic variance).

Table 5. 912 MHz source counts in SCORPIO field. The columns represent: (1) flux density bin interval ΔS in mJy, (2) flux density bin centre S in mJy, (3) number of catalogued sources N in each flux density bin, (4) corrected number of sources N_{corr}, (5) uncorrected normalized differential source counts ($S^{2.5}dN/dS$), (6) corrected normalized differential source counts ($S^{2.5}dN/dS|_{corr}$) with statistical (7) and total (8) uncertainties.

ΔS (mJy)	S (mJy)	N	N_{corr}	$S^{2.5}dN/dS$ (Jy$^{1.5}$sr^{-1})	$S^{2.5}dN/dS\|_{corr}$ (Jy$^{1.5}$sr^{-1})	σ_{stat}	σ_{tot}
0.23	0.50	111	1640.15	0.23	3.45	0.33	0.58
0.37	0.79	409	2183.64	1.72	9.16	0.43	1.10
0.58	1.26	623	1544.04	5.22	12.93	0.50	1.47
0.93	2.00	700	988.56	11.69	16.51	0.56	1.83
1.47	3.16	600	683.18	20.00	22.77	0.87	2.59
2.33	5.01	507	541.79	33.72	36.03	1.55	4.22
3.69	7.94	354	370.61	46.97	49.17	2.51	6.07
5.85	12.59	287	297.43	75.98	78.74	4.46	10.09
9.27	19.95	204	210.18	107.76	111.03	7.82	15.67
14.69	31.62	146	149.81	153.88	157.89	12.48	23.68
23.29	50.12	84	85.92	176.65	180.68	19.50	32.96
36.90	79.43	60	61.22	251.76	256.89	33.38	53.75
58.49	125.89	55	56.02	460.46	468.98	63.84	101.74
157.74	223.87	46	46.77	602.18	612.27	90.02	141.26
314.73	446.68	16	16.25	590.32	599.37	149.02	219.10
3350.11	1584.89	8	8.11	657.56	666.73	241.78	348.37

As can be seen, the measured source counts as a function of the source flux density are consistent with the trend reported in other surveys carried out far from the Galactic plane (e.g. see Katgert 1988; Hopkins et al. 2003 and references therein). The discrepancies observed assuming a spectral index α=−0.7, ranging from 15% to 20%, are within the quoted systematic uncertainties. The presence of our Galaxy is also expected to play a role in this comparison. Galactic sources indeed contribute to the overall source counts, although with a smaller fraction (∼5% at least from the analysis presented in Section 5.1). An overdensity effect (∼10-15%), reported for example by Cavallaro et al. (2018), can not however be clearly identified, being of the same order of the reported uncertainties.

For the sake of completeness we derived the source counts in a region outside the Galactic plane (|b|>2) following the same procedure described above and using an updated response matrix, parametrized on the considered mosaic region. No significant differences (within few percent) were found with respect to the source counts obtained over the full mosaic, suggesting that the majority of the unclassified sources have an extragalactic origin.

5 SOURCE CLASSIFICATION

5.1 Search for known Galactic objects

We cross-matched the ASKAP SCORPIO source catalogue with different astronomical databases to search for possible associations with known Galactic objects. We restricted the search to the following types of objects:

- *Stars*: associations searched in the SIMBAD Astronom-

Table 6. Number of sources from different astronomical catalogues (see text) associated to ASKAP SCORPIO radio sources.

Obj. Type	Catalogue	r_{match} (")	$n_{matches}$	$n^{random}_{matches}$	Confirmed objects
Star	SIMBAD	4	20	2.3±0.3	13
	WR Cat.	4	0	0	0
	GAIA DR2	2	933	874.2±9.6	0
Pulsar	ATNF Cat.	8	21	0	21
PNe	HASH	8	38	0	27
HII regions	WISE	32	67	0	35
All			146*		96

* GAIA matches not included in the final count.

ical Database[11], in the Galactic Wolf-Rayet Star Catalogue[12] (Rosslowe & Crowther 2015) and in the Gaia data release 2 catalogue (Brown et al. 2018);

- *Pulsars*: associations searched in the ATNF Pulsar Catalogue[13] (Manchester et al. 2005) (version 1.63);
- *Planetary Nebulae (PNe)*: associations searched in the Hong Kong/AAO/Strasbourg H-alpha (HASH) Planetary Nebula Database[14] (Parker et al. 2016);
- *HII regions*: associations searched in the WISE Catalogue of Galactic HII regions[15] (Anderson et al. 2014).

Extended objects, such as the supernova remnants (SNRs) listed in the Galactic SNR catalogue[16] by Green (Green 2019), were not considered in this analysis. Possible associations and new detections will be reported in a future work dedicated to SCORPIO extended sources.

We summarize the cross-match results in Table 6. The number of associations found for each catalogue is reported in column 4 while the expected number of false matches is given in column 5. These were estimated with the same procedure described in Section 3.2, i.e. evaluating the number of matches found within the chosen radius in several "randomized" catalogues. The search radius considered for the matching, reported in column 3, corresponds to the maximum statistical significance of the match signal above the background. The number of objects labelled as "confirmed" in the astronomical databases is reported in column 6.

Only 146 objects were associated to known classes of Galactic objects, corresponding to ∼4% of the total number of SCORPIO catalogued sources. The vast majority of the catalogued sources are thus labelled as not classified. A 2D map showing the positions of both classified and unclassified sources is reported in Fig. D1 (available in the online version of this paper).

[11] http://simbad.u-strasbg.fr/simbad/
[12] http://pacrowther.staff.shef.ac.uk/WRcat/index.php
[13] https://www.atnf.csiro.au/research/pulsar/psrcat/
[14] http://202.189.117.101:8999/gpne/dbMainPage.php
[15] http://astro.phys.wvu.edu/wise/
[16] http://www.mrao.cam.ac.uk/surveys/snrs/

5.1.1 *Stars*

Inside the SCORPIO ASKAP region, we selected 10628 stars in the SIMBAD database and 19 Wolf-Rayet stars in the Rosslowe & Crowther (2015) catalogue. These were cross-matched to ASKAP source components within a match radius of 4" in sky coordinates. Since the Gaia catalogue is densely populated (more than 9×10^6 entries found in the SCORPIO region) we lowered the search radius to 2", comparable to the positional uncertainties obtained in ASKAP. We found 20 associations in SIMBAD, among them 7 YSO (1 confirmed, 6 candidates), and no associations with Wolf-Rayet stars up to a matching radius of 32". SIMBAD matches are expected to be real as the estimated number of chance matches is 2.3±0.3 (see Table 6). The associations found with Gaia DR2 (933) are instead dominated by random matches and will not be further considered. A list of the associated objects found is reported in Table E2 (available in the online version of this paper). The reported classification was investigated with infrared and optical data. Details are reported below:

(i) `SSTGLMC G343.7018+00.0861`: invisible in optical and near-IR; clear but not particularly red in the mid-IR. Not immersed in a region of star formation. YSO candidate classification is premature. Could well be extragalactic.

(ii) `IRAS 16495-4140`: likely a YSO. It is a small clump of stars of which two dominate in the near-IR (2MASS). Together they are bright and red in the mid-IR (WISE; not covered by Spitzer).

(iii) `2MASS J17062471-4156536`: classified as a YSO candidate with star-forming activity (and dark cloud) nearby. Could be extragalactic. Invisible in the optical but bright (and red) in 2MASS. Not particularly red in Spitzer and WISE.

(iv) `SSTGLMC G344.2155-00.7460`: only detected in the mid-IR, faintly. There is nothing to suggest otherwise that this is a background AGN. It is not near star-forming complexes and it is next to darker areas of extinction, i.e. viewed through a relatively more transparent region. The YSO classification is questionable.

(v) `IRAS 16534-4123`: likely extragalactic. It is exceedingly faint in optical and very bright in WISE.

(vi) `[MHL2007] G345.0052+01.8209 1`: Class I protocluster. Clump of red stars in 2MASS, no detection in optical, embedded within a diffuse background emission seen with Spitzer (GLIMPSE) and saturating in WISE.

(vii) `HD 326586`: F8 star, bright GALEX (UV) source.

(viii) `SSTGLMC G342.6544-00.3827`: faint, red. Detected in optical and near-IR, not particularly bright or red in mid-IR. Not necessarily a YSO, and no indications that it should be radio-loud. Could well be a background AGN.

(ix) `IRAS 16472-4401`: related by SIMBAD with an IRAS source, undetected in 2MASS. Close to the source's sky position (≈6 arcsec), a YSO was detected by the ATLASGAL survey at 870 μm (Urquhart et al. 2018).

(x) `2MASS J16504054-4328122` (`IRAS 16470-4323`): while SIMBAD classes it as an AGB star, there is no direct evidence for this. It is strangely yellow in the DECaPS (five-band optical and near-infrared survey of the southern Galactic plane with the Dark Energy Camera (DECam) at Cerro Tololo), unlike any other object around it. It is red in 2MASS but again yellow in Spitzer and WISE. The

Gaia data are marginal, so we cannot completely exclude an extragalactic nature.

(xi) `HD 326392`: classified as B8 star ≈830 pc far (Brown et al. 2018). At the stellar distance, the measured flux of HD 326392 corresponds to a radio luminosity of $\approx 6\times10^{17}$ ergs s^{-1} Hz^{-1}, more than one order of magnitude higher than CU Vir ($\approx 3\times\ 10^{16}$ ergs s^{-1} Hz^{-1}, Leto et al. 2006), a magnetic late B type star well studied at radio regime. The radio luminosity of HD 326392 is instead more comparable to those of strong magnetic stars of B2 spectral type, level ≈10 kG and luminosity close to 10^{18} ergs s^{-1} Hz^{-1} (Leto et al. 2017, 2018). This suggests HD 326392 as a possible strong magnetic star.

(xii) `2MASS J17122205-4230414`: fairly red but not too faint in the optical, bright in the mid-IR. As such it is isolated, the post-AGB classification seems more likely than a YSO (as listed in SIMBAD). It is found to be slightly extended and classified as a planetary nebula by (Suarez et al. 2006) with high confidence, though their optical spectrum shows no trace of [OIII].

(xiii) `TYC 7872-1355-1`: Anonymous star, but in a reflection nebula.

(xiv) `MSX6C G346.4809+00.1320`: YSO, Class 0 (invisible in near-IR) with a 6.7-GHz methanol maser detection by Gaylard & MacLeod (1993) and a single 100% polarized 1665-MHz OH maser peak by Caswell & Haynes (1983).

(xv) `2MASS J17074166-4031240`: likely a YSO. It is invisible in the optical but clear and red in 2MASS; however, the mid-IR emission comes mainly from the bright rim (photodissociation region) of a cloud/HII region immediately to its side, most likely the origin of the radio emission.

(xvi) `CD-38 11343`: Classified as "double star" (er* (M3Ve+M4Ve)) in SIMBAD. Eruptive pair of M dwarfs at 15 pc, with likely expected variability also in radio.

(xvii) `IRAS 17056-3930`: very faint red optical, but bright(ish) red near-IR and mid-IR source. However, it is very isolated, there is nothing like it within at least 5 arcminute radius in a field of stars with the nearest sign of star formation activity about 8 arcminutes away. Further investigations are needed to address its nature.

(xviii) `IRAS 17056-3916`: no detection in optical or near-IR, but very red mid-IR source; possibly unresolved. It is located right at the edge of a dark cloud, which could suggest it is a YSO or explain why it is not seen in the optical. Further investigations are needed to confirm if of extragalactic origin.

(xix) `Cl* NGC 6318 PCA 7229`: Classified as "star in cluster" in SIMBAD. This might in fact be the `AGAL G347.919-00.762` YSO, detected in Spitzer data.

(xx) `TYC 7873-953-1`: radio source generically classified by the SIMBAD database as star. This is associated with a visible source about 1.2 kpc far (Brown et al. 2018). Further, this was discovered as a variable radio source at 1.4 GHz from NVSS data (Ofek & Frail 2011).

We compared the matches found with those obtained in pilot observations of the Scorpio field with ATCA at 2.1 GHz. Only 2 of the 10 star associations reported in Umana et al. (2015) are retrieved also in the ASKAP map. Due to a lack of sensitivity, no radio sources are detected in the direction of the two Wolf-Rayet stars (`HD 151932`, `HD 152270`) previously detected in ATCA.

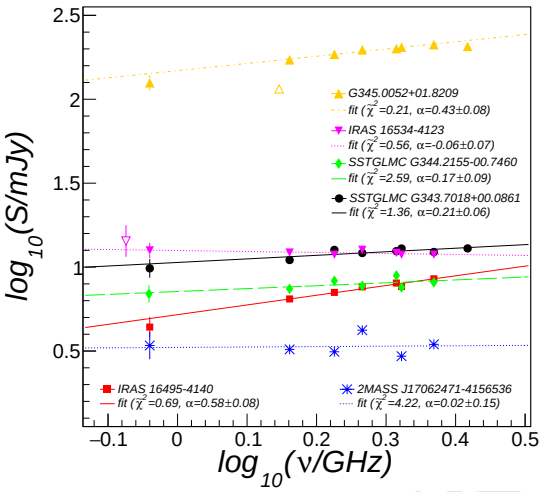

Figure 8. Spectral data of Scorpio sources associated to stars in the SIMBAD database, obtained using ASKAP and ATCA data (filled markers) and previous MGPS and NVSS observations (open markers). The power-law fits are reported with coloured lines.

For 6 associated objects, shown in Fig. 8 and reported as top entries in Table E2, we were able to derive a spectral index measurement (column 14) using Scorpio ASKAP and ATCA, MGPS and NVSS data (see Section 4.2). Among them we have 4 Young Stellar Object (YSO) candidates with fitted spectral index α: 0.21±0.06 (`SSTGLMC G343.7018+00.0861`), 0.02±0.15 (`2MASS J17062471-4156536`), 0.17±0.09 (`SSTGLMC G344.2155-00.7460`), 0.43±0.08 (`[MHL2007] G345.0052+01.8209 1`). Taking into account the reported uncertainties, these values are generally consistent with the spectral indices expected in optically thin free-free emission processes from ionized gas. According to Scaife (2012); Ainsworth et al. (2012); Anglada et al. (2018), the free-free radio emission at centimetre wavelengths is ascribed to outflow processes (e.g. thermal jets) causing the required gas ionization, particularly in the earliest protostellar stages (Class 0 and Class I). The resulting YSO radio spectral indices α are expected in the range $-0.1<\alpha<1.1$ but their values depend on the protostar evolution. For example in collimated outflows, typical of early protostar stages, a radio spectral index $\alpha \sim 0.25$ is favoured, while, for standard conical jets, spectral indices around 0.6 are expected (Reynolds 1986; Anglada et al. 1998). Existing measurements mostly fall in the above range although in some cases the observed spectral indices (< -0.5) suggest a contribution from non-thermal processes (Ainsworth et al. 2012). Our spectral index measurements are found within the range expected from free-free emission. Additional radio data at different frequencies are however needed to further constrain the dominant emission mechanism.

5.1.2 Pulsars

The ATNF Pulsar database has 58 catalogued pulsars inside the Scorpio region. We carried out a search for possible as-

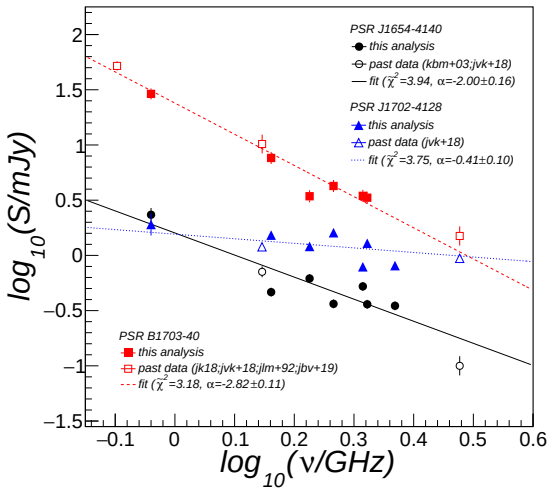

Figure 9. Spectral data for J1654-4140 (open black dots), B1703-40 (open red squares) and J1702-4128 (open blue triangles) pulsars reported in the ATNF pulsar catalogue: kbm+03 (Kramer et al. 2003), jvk+18 (Jankowski et al. 2018), jk18 (Johnston and Kerr 2018), jlm+92 (Johnston et al. 1992), jbv+19 (Jankowski et al. 2019). ASKAP and ATCA spectral data obtained in this work are shown with filled markers. Single power-law fits are reported with solid, dashed and dotted lines for the three sample pulsars.

sociations with SCORPIO source components, finding 21 associations within a matching radius of 8" and a number of chance matches compatible with zero.

In Table E3 (available in the online version of this paper) we report the full list of matched objects. Four of these (J1654-4140, B1703-40, J1702-4128, J1702-4217), shown as top entries in the table, have spectral index information (column 14) that can be obtained from ASKAP and ATCA data only. Column 12 represents the spectral index reported in the ATNF catalogue from measurements at 0.8, 1.4 and 3.0 GHz (Jankowski et al. 2018, 2019; Kramer et al. 2003; Johnston and Kerr 2018; Johnston et al. 1992). Flux density measurements, available in the literature for three of them (J1654-4140, B1703-40, J1702-4128), are reported in Fig. 9 with open markers. New measurements, obtained in this work, are shown with filled markers. Both ASKAP and ATCA fluxes compare well to existing data, allowing us to derive a new spectral index measurement for all three pulsars. Fit results are shown in the figure with solid, dashed and dotted lines. The steep spectral index values found for J1654-4140 and B1703-40, reported in Table E3 (column 14), are compatible with the distribution of pulsar spectral indices compiled in Maron et al. (2000) ($\langle\alpha\rangle$=−1.8±0.2). The flat spectrum of J1702-4128, confirmed by our ASKAP and ATCA observations, supports the hypothesis of a pulsar wind nebula (PWN) as the origin of the radio emission. This was investigated by Chang et al. (2008) to explain the nature of the X-ray emission from Chandra CXOU J170252.4-412848 but no conclusive evidence was reached. Future ASKAP EMU and POSSUM data might give further evidence for a PWN if this source is linearly polarized.

5.1.3 *Planetary Nebulae*

Within our surveyed area, HASH has 60 PNe[17] that were cross-matched to ASKAP catalogued sources at different matching radii. A number of 38 associations were found assuming a radius of 8". 27 of the 38 matches correspond to confirmed PN objects. The number of chance matches found is compatible with zero. We visually inspected the 5 confirmed PNe (MPA J1715-3903, MPA J1717-3945, MPA J1654-3845, MPA J1644-4002, PHR J1709-3931) that were not cross-matched to any ASKAP source. In the direction of the first four PNe there are no radio sources in the map. A faint radio source is instead found in the direction of PHR J1709-3931 but it is detected at an S/N of only 4.1.

A full list of associated PNe is reported in Table E4 (available in the online version of this paper). With ASKAP we detected the 9 HASH PNe studied with ATCA 2.1 GHz observation in Ingallinera et al. (2019). ATCA flux measurement is however reported in this study for only 5 PNe (1 confirmed: IRAS 16515-4050, 4 candidates: MPA J1654-4041, PHR J1654-4143, Pre 11, DGPK 2), shown in Fig. 10 and listed as top entries in Table E4. Four PNe were fitted with simple power-law models (labelled as "PL" in Fig. 10) as their radio spectra do not show evidence of spectral curvature in the studied frequency range. Although the fit models are not highly statistically significant, the results constitute a first measurement of the average spectral index for these objects as no other measurements are available in the literature.

The radio spectrum of IRAS 16515-4050 PN cannot be described by a single power-law model and was instead fitted with a thermal free-free emission model S_{ff}:

$$S_{ff}(\nu;T_e,\mathrm{EM},\Omega) = F(\nu;T_e)(1-e^{-\tau(\nu;T_e,\mathrm{EM})})\Omega \quad (17)$$

$$\tau(\nu;T_e,EM) = 3.014\times10^{-2}T_e^{-1.5}\left(\frac{\nu}{\mathrm{GHz}}\right)^{-2} g_{ff}(\nu;T_e)\,\mathrm{EM} \quad (18)$$

$$g_{ff}(\nu;T_e) = \ln\left[4.955\times10^{-2}\left(\frac{\nu}{\mathrm{GHz}}\right)^{-1}\right] + 1.5\ln T_e \quad (19)$$

where $F(\nu;T_e)$ is the Planck function, T_e is the electron temperature, EM is the emission measure and Ω is the source solid angle. A good fit of the data was obtained with T_e fixed to 10^4 K and the other parameters free to vary[18]: EM=6.53±0.76×10^6 cm^{-6}pc and Ω=2.40±0.21×10^{-11} sr (angular size $\theta\sim1$").

For the rest of catalogued PNe we were able to estimate the spectral index by combining our measurements with existing ones at 843 MHz (Murphy et al. 2007) (MOST), 1.4 GHz

[17] This number refers to the number of PNe (32 True PN, 6 Likely PN, 7 Possible PN, 15 New Candidates) listed in the online HASH database version 4.6 (http://202.189.117.101:8999/gpne/dbMainPage.php) at the time of writing of the paper and found inside the source finding region. If we also consider the mosaic edges the PN count increases to 67 (36 True PN, 7 Likely PN, 8 Possible PN, 16 New Candidates).

[18] We considered an average value with respect to measured PN electron temperatures found in the range 5000-15000 *K* (e.g. see Zhang et al. 2014 for results on a sample of 48 Galactic PNe).

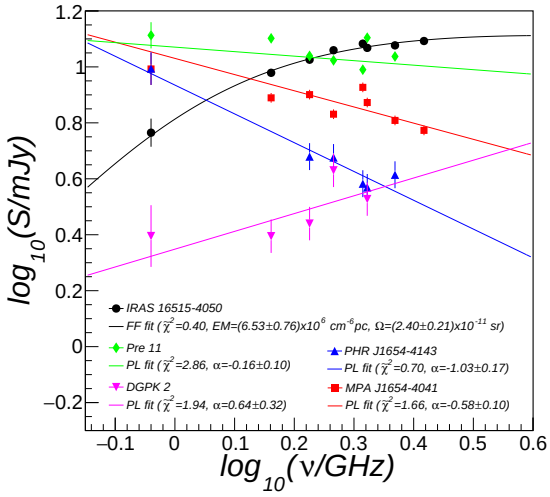

Figure 10. Radio continuum spectra for five PNe obtained using ASKAP and ATCA observations.

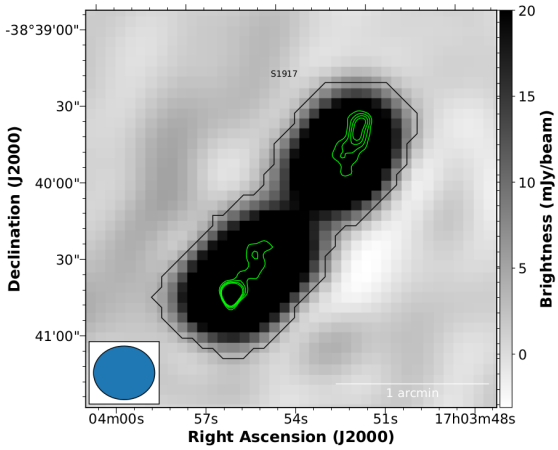

Figure 11. A sample radio galaxy classified with high-confidence in both the ASKAP Scorpio map (colour scale and solid black contour) and in the VLASS survey (superimposed solid green contours). The ellipse at the bottom left indicates the ASKAP synthesized beam size.

(Condon et al. 1998; Condon and Kaplan 1998) (VLA), 4.8 GHz (van de Steene and Pottasch 1993) (ATCA). Some of them, obtained using 843 and 912 MHz measurements only, are clearly unreliable due to the limitations discussed in Section 3.3.3.

The spectral indices obtained with data at higher frequencies are found in general agreement with the expected nature of the emission in PNe, i.e. thermal free-free radiation due to electron-ion interactions in the nebula shell (Kwok 2000). The expected spectral indices, however, vary considerably depending on the thermal and electron density scenario, roughly ~ -0.1 in an optically thin regime and positive up to ~ 2 (Pottasch 1984) for optically thick PNe. The first scenario is likely in place in `MPA J1654-4041`, `PHR J1654-4143`, `Pre 11`, `Vd 1-5` and `Vd 1-6` for which we observed negative spectral indices. The second scenario seems favoured for some other detected PNe, e.g. `IRAS 16515-4050`, `DGPK 2`, `PM 1-119` and `PM 1-131`. Due to the limited number of radio observations available, the precision achieved on the spectral indices does not allow us to constrain the PN nature and corresponding emission mechanism. Deeper analysis, possibly in combination with IR data as in Fragkou et al. (2018); Ingallinera et al. (2019), will be therefore performed in the future once new ASKAP observations with different frequency bands become available.

5.1.4 HII regions

Within the Scorpio region used for source finding, we found 356 Galactic HII regions catalogued in Anderson et al. (2014)[19]. 256 of these were classified by these authors as "known" (i.e. objects confirmed by Anderson et al. 2014 or in previous studies, including radio quiet HII regions), with the rest as candidates (including those closely located to a known HII region). Their sizes range from 0.2" to ~23 arcmin with a median of ~1 arcmin. Within a matching radius of 32" we found 67 HII regions associations[20]. The matched HII regions have a reported radius between 12" and 100" (average radius ~52"). From a visual inspection, we were able to confirm ~90% of the matches found in the automated analysis.

Thirteen HII regions were detected in both the ASKAP and ATCA maps. We were able to determine a first measurement of the radio spectral index for 9 of them (6 confirmed objects and 3 candidates). The remaining ATCA sources have either an unreliable spectral fit, due to noisy subband data, or an unclear association with ASKAP data. For instance, ASKAP source associated to `G344.993-00.265` is located close to another, more compact, HII region (`G344.989-00.269`). The higher resolution of ATCA observations allows us to distinguish the two sources when estimating their flux densities. This is not the case for ASKAP data in which the two sources are blended. Future ASKAP observations will provide the required sensitivity, resolution and additional spectral data to refine and extend this analysis. Finally, an additional spectral index measurement was obtained for `G347.921-00.763` using MGPS and NVSS data. More details for each source are reported in Table E5 (available in the online version of this paper).

5.2 Extragalactic sources

A large number of the extracted sources (~3800 source islands, >95% of the catalogue) are not classified or associated to a known astrophysical object. Following the findings reported in previous radio surveys carried out in the Galactic plane (Wang et al. 2018; Cavallaro et al. 2018) and the comparison with extragalactic source counts reported in

[19] The number of HII regions falling in the full ASKAP mosaic, including borders, is 382, as reported in paper 1 (Umana et al. in prep.).

[20] The number of HII regions detected in ASKAP is 261, as reported in paper 1 (Umana et al. in prep.), if we also consider the mosaic borders and the extended sources that were excluded from this catalogue.

Table 7. Number of radio galaxies identified in the Scorpio ASKAP mosaic per number of islands and labelled according to the degree of confidence reached in the identification (see text).

# islands	Degree of confidence	
	LOW	HIGH
1	103	131
2	10	28
3	0	5
All	113	164

Section 4.3, we may reasonably expect that the majority of them are extragalactic objects. A search in the NASA/IPAC Extragalactic Database (NED)[21] returned only 20 known objects classified as galaxies (G). Two of them (`2MASS J17172771-4306573`, `2MASX J16463421-3903086`) are found associated to SCORPIO catalogued sources. Another one (`2MASS J17162433-4225102`) is likely associated to a faint non-catalogued ASKAP radio source (S/N=3.7). For the rest, there are no indications for a co-spatial radio emission at the current map sensitivity.

We report here a preliminary analysis to increase the number of classified sources and provide the basis for more advanced studies to be done in the future. Indeed some of the unclassified source islands are found to have a bipolar morphology resembling those of radio galaxy lobes or can be visually associated to neighbor islands connected by a radio jet-like emission. We can therefore visually inspect the ASKAP map to search for this kind of object and label them as candidate radio galaxy. Since a precise identification using morphological considerations only is currently severely limited by the resolution of our ASKAP map, we also considered the ATCA map which provided the needed resolution to address some of the unclear identifications. Results are reported in Table 7.

A number of 277 candidate radio galaxies were identified. None of them are associated to known NED extragalactic objects. The majority was found associated to one island detected in the catalogue (e.g. other components are either not visible or below the detection threshold) and only a few associated to two or three islands (which may correspond to a single source). The number of source islands associated to the candidate galaxy do not always have a 1-to-1 correspondence to the physical components (e.g. core, lobes). In many cases the latter are in fact visible inside a single island.

For almost half of the cases there were no strong indications whether the radio morphology would suggest a radio galaxy. These have been labelled as candidates with lower degree of confidence in Table 7. About 70 radio galaxy candidates, lying north of Dec=−40 deg, were visually inspected in the QuickLook data release of the VLASS 2-4 GHz survey (Lacy et al. 2020). Only two of them (one is reported in Fig. 11) were firmly confirmed as radio galaxies from their morphology, while the rest are resolved out or only showing the core component. Given the resolution limitations already discussed, future ASKAP observations at higher resolution will be needed to confirm the nature of these candidates.

Spectral information, measured only for 74 source components found in candidate radio galaxy islands, may provide additional hints for these studies, at least for a subset of the sources. Following the classification scheme reported in Zajaček et al. (2019), 62 of them have a lobe-like steep index ($\alpha < -0.7$), 6 are found with a jet-like index ($-0.7 \leq \alpha \leq -0.4$) and 6 with a flatter core-like index ($\alpha > -0.4$).

5.3 Unclassified sources

The remaining unclassified sources (3588), which still constitute the major part of the catalogue (∼87%), cannot be classified on the basis of their morphology given that the majority (∼95%) does not present any internal structure at the resolution of ASKAP map. For these, the radio spectral index and the correlation with observations at different wavelengths can provide valid hints. The radio-infrared correlation, in particular, was suggested by many authors (e.g. see Ingallinera et al. 2014; Fragkou et al. 2018; Akras et al. 2019) as a powerful tool for the identification of different classes of Galactic objects. Radio continuum emission traces the ionized part of the nebula, whereas infrared traces excited gas and the dust. In this context, the combination of infrared color indices obtained with different wavelength filters (from few μm to hundreds of μm) has been a widely used technique to probe IR emission from different components (Nikutta et al. 2014; Anderson et al. 2012). For example, the correlation of far-infrared to mid-infrared colors allows to compare emission from cold and warmer dust components. The ratio between IR fluxes at 12 μm and 8 μm is instead sensitive to the emission from PAHs (polycyclic aromatic hydrocarbons).

As discussed in Section 3.2.3, about 2500 unclassified sources (∼70%) do not have infrared counterparts within a search radius equal to the ASKAP synthesized beam size. These are expected to be mostly extragalactic sources and pulsars. For 607 of these, we obtained a radio spectral index, reported in Fig. 13 (solid black histogram), that will be combined with additional observables in future classification studies. Bearing the cross-match limitations in mind (highlighted in Section 3.2.3), we will carry out the following analysis to the other 284 of the unclassified sources found with infrared counterparts within 8", of which 67 have both the radio spectral index information and measured radio-infrared correlation parameters.

5.3.1 Infrared-radio colors

We report in Fig. 12 a series of correlation plots of selected infrared-infrared and infrared-radio color indices for different IR wavelengths (3.4 μm, 4.6 μm, 8 μm, 12 μm, 22 μm, 70 μm). Color $c_{i,j}$ is defined as the magnitude difference between measured fluxes S_i and S_j in band i and j where $\lambda_j > \lambda_i$, e.g. $c_{i,j} = 2.5\log_{10}(S_j/S_i)$. As only a subset of the available colors are independent, we selected the most effective ones, in terms of source discrimination power, reported in the literature (Nikutta et al. 2014; Anderson et al. 2012): $c_{3.4,4.6}$,

[21] The NASA/IPAC Extragalactic Database (NED) (`http://ned.ipac.caltech.edu`) is operated by the Jet Propulsion Laboratory, California Institute of Technology, under contract with the National Aeronautics and Space Administration.

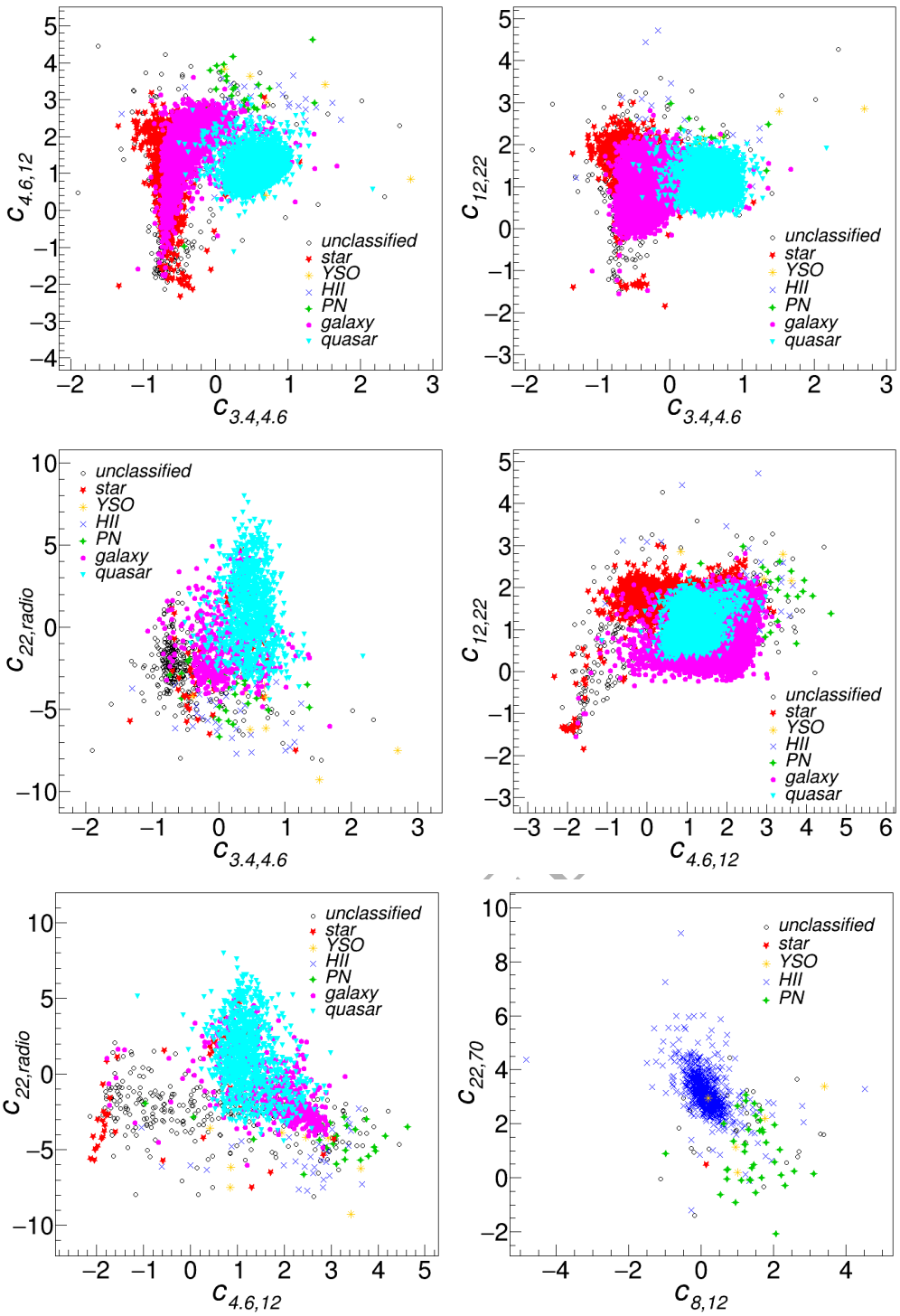

Figure 12. Scatter plots of selected infrared-infrared or infrared-radio colors for different infrared bands (3.4 μm, 4.6 μm, 12 μm, 22 μm, 70 μm). Unclassified objects are shown with gray smaller dots while pre-classified sources with colored markers (HII regions: blue crosses, PNe: green diamonds; stars: red stars; YSOs: orange asterisks; galaxies: purple dots, QSO: cyan triangles).

$c_{4.6,12}$, $c_{12,22}$, $c_{8,12}$, $c_{22,70}$. An additional color ($c_{22,\mathrm{radio}}$) was considered to include the radio information. Unclassified objects are shown with open black dots, while pre-classified sources found in the SCORPIO mosaic with colored markers (HII: blue crosses, PNe: green diamonds; stars: red stars; YSOs: orange asterisks; galaxies: purple dots).

We superimposed data for different classes of objects taken from previous radio surveys crossmatched to the aforementioned infrared surveys. Radio star data (shown as red stars) at 843 MHz and 1.4 GHz are taken from Kimball and Ivezić

(2008)[22] and from Wendker (1995). Data for galaxy and QSO with point-like morphology at 1.4 GHz (shown respectively with purple dots and cyan triangles) are taken from Kimball and Ivezić (2008). Additionally, we included infrared data for stars, galaxies and quasars from Clarke et al. (2020), taking only sources reported with classification probability equal to 1 and requiring infrared fluxes above the AllWISE 5σ limits for all bands (Cutri et al. 2013). HII regions (blue crosses) and PNe (green diamonds) at 843 MHz and 1.4 GHz data are taken from the Anderson et al. (2014) and HASH (Parker et al. 2016) databases, respectively. Radio data at 5 GHz for YSO (orange asterisks) are taken from Urquhart et al. (2009). Pulsar data from the ATNF database (Manchester et al. 2005) were also considered but since no match was found with IR data they were not reported in Fig. 12.

From Fig. 12 we observe that most color correlations provide valuable information to separate Galactic and extragalactic sources. Longer wavelength bands are found more sensitive to object identity information for classification purposes. For example known Galactic objects tend to have larger $S_{12,22}/S_{3.4,4.6,radio}$ flux ratios on average compared to galaxies. From the data shown in the bottom right panel, one may be tempted to conclude that the sole presence of an associated 70 μm emission is a clear indication of the source's Galactic origin. This is rather due to a lack of reference data for extragalactic background objects in this portion of the parameter space. Indeed, far infrared emission (also at 70 μm) from several nearby galaxies was reported in different works (e.g. see Dale et al. 2012) and expected from our calculations[23].

Reference data have some limitations to be considered for further analysis. First, the currently available radio data are obtained at slightly different frequencies (843 MHz, 1.4 GHz, 5 GHz) with respect to the ASKAP SCORPIO data (912 MHz). The introduced spread in the IR/radio colors is expected to be negligible for Galactic sources with thermal emission or flat spectra. A correction for sources with steeper spectra (expected of the order of 0.5 and 1.8 at 1.4 and 5 GHz, respectively, with α=−1) is however not possible as the spectral index information is only available for very few sources. A second limitation is that the source parameter data have many missing values for multiple reasons that can not easily be distinguished from one another without an in-depth revision of the external catalogue data. This prevented us from encoding and imputing missing information in an effective way. For example, some catalogues do not always provide match information for all IR bands, e.g. WISE W1 and W2 information is missing in the HII region and PN catalogues, but we may expect for a subset of these sources

[22] Catalogue data available at http://www.aoc.nrao.edu/~akimball/radiocat_2.0.shtml

[23] Following Silva et al. (1998); Michałowski et al. (2008, 2010); Iglesias-Páramo et al. (2007) we computed the expected 70 μm emission as a function of redshift for different SED models and compared it with the Hi-GAL detection threshold of ∼0.5 mJy (Molinari et al. 2016). For radio fluxes close to the catalogue detection threshold (∼5 mJy) only galaxies (z <0.6) with specific SED models can be detected. Above the ASKAP detection threshold we expect galaxies to be detectable at all redshifts and, thus, to populate the corresponding parameter space in Fig. 12

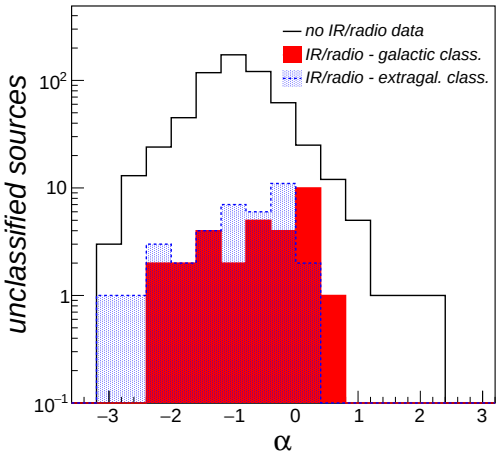

Figure 13. Measured spectral index for unclassified sources. The solid black line histogram includes unclassified sources for which no combined infrared-radio parameter data are available. Filled red and shaded blue histograms include unclassified sources that were classified as Galactic and extragalactic sources, respectively, in the combined infrared-radio analysis.

an emission at these wavelengths[24]. Flux information may also be missing for some sources either because the reference survey covers a limited portion of the sky (e.g. radio galaxy data obtained in extragalactic surveys do not have 8 and 70 μm information) or because the source is not emitting or below the detection threshold. We eventually removed sources with missing data (e.g. using listwise deletion), reducing the sample size usable for analysis.

5.3.2 *Classification analysis*

We attempted to perform a simple source classification analysis to identify Galactic source candidates using four color parameters ($c_{3.4,4.6}$, $c_{4.6,12}$, $c_{12,22}$, $c_{22,\mathrm{radio}}$) for which we have the largest availability of data for all bands. The resulting training sample (∼1650 sources) is unbalanced by a factor 10 towards extragalactic objects. A decision tree classifier was then trained on this dataset and tested on the unclassified sample (284 sources). The optimal tree maximum depth size (3) was determined by comparing classification performances on multiple random validation samples. On the full training sample we obtained these classification metrics (recall/precision/F1-score): 0.99/0.97/0.98 for extragalactic sources and 0.69/0.89/0.78 for Galactic sources.

[24] We visually inspected some of the catalogued HII regions in all WISE bands. The infrared emission in bands W1 and W2 was effectively found absent or not correlated with the W3 and W4 emission but we cannot exclude such a correlation for the rest of catalogued objects that were not inspected. In fact in Assef et al. (2018) the authors conservatively removed the areas of the sky around WISE HII regions to eliminate the Galactic source background when searching for potential AGN in W1 and W2 bands. An emission at these shorter wavelengths, albeit smaller compared to W3 and W4 bands, can be therefore present and was indeed observed in some of the HII regions catalogued by CORNISH (Purcell et al. 2013) (for example in G019.6062-00.9018)

As expected from Fig. 12, stars are the most misclassified type of object (∼70% of the wrong identifications). From the decision rules it can be seen that one of the color parameter ($c_{12,22}$) is not effectively used for the classification. Decision rules can be expressed in pseudocode as follows:

```
if c_{22,radio} ≤ −4.05 then
    Galactic
else
    if c_{4,6,12} ≤ −0.51 then
        if c_{3,4,4,6} ≤ −0.68 then
            extragalactic
        else
            Galactic
        end
    else if c_{4,6,12} > −0.51 & c_{4,6,12} ≤ 2.97 then
        extragalactic
    else
        Galactic
    end
end
```

The trained tree classifies 99 sources as Galactic objects, 75 of them with classification probability larger than 90%. In Fig. 13 we report the measured spectral indices for a subset (30) of them (filled red histogram) in comparison with sources classified as extragalactic (shaded blue histogram). Unfortunately, we do not have enough training data to classify different types of Galactic objects. Nevertheless, it is interesting to inspect the predictions of other classifiers (employing additional IR colors) on our data. Akras et al. (2019), for example, obtained a PN classification efficiency of ∼50% and a contamination from mimics (HII, stars, YSO) ranging from 30% to 40% using these color cuts:

$$\begin{aligned} &J-H<1.10,\ W1-W4\geq 7.87 \quad \text{or} \\ &J-H<1.31,\ K-W3\geq 6.42 \end{aligned} \tag{20}$$

No unclassified source was found to satisfy both cuts. In particular the second condition (involving WISE colors) of both cuts was not fulfilled by any source passing the first condition.

Anderson et al. (2012) reported an HII region classification efficiency better than 95% with a PN contamination around 20% requiring the following criteria (at least one of them):

$$\begin{aligned} &\log_{10}(S_{12}/S_8)<0.3 \\ &\log_{10}(S_{22}/S_8)<1 \\ &\log_{10}(S_{70}/S_{12})>1.3 \\ &\log_{10}(S_{70}/S_{22})>0.8 \end{aligned} \tag{21}$$

We found that 47 sources, previously classified as Galactic objects, satisfy the first two criteria, while only 2 are passing all criteria (requiring emission at 70 μm). These are likely new HII region candidates to be explored and confirmed in follow-up studies.

To make further advances we will need to individually assess the reliability of each radio-IR association (currently quoted in Section 3.2.3 as ∼60% with a match radius of 8") and possibly increase the sample of pre-classified objects to constrain the parameter space with a higher degree of confidence. Data validation efforts have already started and will be reported in a future paper.

6 SUMMARY

We have analyzed ASKAP Early Science observations of the SCORPIO field (∼40 deg^2, σ_{rms}>200 μJy/beam, 24"×21" angular resolution) at 912 MHz and produced a first catalogue of compact radio sources and their components using the CAESAR source finder. We summarize below the main results:

(i) The catalogue contains 4144 source components with flux densities ranging from 3.9 Jy down to 0.3 mJy. About ∼87% were detected at a significance higher than 5σ. From simulations, we estimated a catalogue completeness of at least 90% above 5 mJy. The differential source counts are compatible with literature data at 1.4 GHz obtained outside the Galactic plane, after taking into account the different observation frequency and analysis systematics. This suggests a majority of extragalactic sources in the catalogue.

(ii) Through comparison with different radio surveys, including our ATCA observations at 1.4 - 2.6 GHz, we estimated the spectral indices for a subset of the catalogued sources (780) finding a median value of $\langle\alpha\rangle=-0.92$ (IQR=0.68) in agreement with previous works within the discussed uncertainties. The higher resolution ATCA data also allowed us to derive a lower limit (∼8%) on the fraction of the extended sources present in the catalogue.

(iii) We cross-matched the source catalogue with different astronomical databases (SIMBAD, HASH, WISE HII regions, Wolf-Rayet catalogue) to search for possible associations to known Galactic objects. Including candidate objects, we have found 20 stars (including 7 YSO), 21 pulsars, 38 PNe, 67 HII regions, providing new spectral index measurements for a subsample of these, detected in both ASKAP and ATCA observations.

(iv) The vast majority (>96%) of the catalogued sources are unclassified, likely dominated by extragalactic background sources. About 300 sources have been identified as radio galaxy candidates from morphological considerations. The remaining sources were analyzed in correlation with existing mid-infrared data, in particular with the AllWISE survey. The majority of the unclassified sources do not have IR counterparts at 12 and 22 μm above IR flux sensitivity levels (∼6 mJy) within the ASKAP beam radius. About one hundred sources found with IR counterparts were preliminarily classified as Galactic objects on the basis of their radio-infrared colors. A summary of the obtained results is reported in Table E1 (available in the online version of this paper).

The source catalogue will be updated before the beginning of the ASKAP Galactic plane survey once that the scheduled Early Science data of the ASKAP SCORPIO field with 36 antennas at three different frequencies (920 MHz, 1296 MHz, 1630 MHz) are available and fully reduced. The multi-frequency data and the expected boost in sensitivity and spatial resolution will enable us to measure the spectral index for all SCORPIO sources, including those located outside the ATCA survey and near the current ASKAP detection threshold, enabling further advances in our classification studies.

ACKNOWLEDGEMENTS

The Australian SKA Pathfinder is part of the Australia Telescope National Facility which is managed by CSIRO. Operation of ASKAP is funded by the Australian Government with support from the National Collaborative Re-

search Infrastructure Strategy. Establishment of the Murchison Radio-astronomy Observatory was funded by the Australian Government and the Government of Western Australia. This work was supported by resources provided by the Pawsey Supercomputing Centre with funding from the Australian Government and the Government of Western Australia. We acknowledge the Wajarri Yamatji people as the traditional owners of the Observatory site.

We thank the authors of the following software tools and libraries that have been extensively used for data reduction, analysis and visualization: ASKAPsoft (Whiting et al. 2019), CAESAR (Riggi et al. 2016, 2019), astropy (Astropy Collaboration et al. 2013, 2018), ROOT (Brun & Rademakers 1996), TOPCAT (Taylor 2005, 2011), ds9 (Joye & Mandel 2003), APLpy (Robitaille & Bressert 2012).

This publication makes use of data products from the Wide-field Infrared Survey Explorer, which is a joint project of the University of California, Los Angeles, and the Jet Propulsion Laboratory/California Institute of Technology, funded by the National Aeronautics and Space Administration. Additionally, this research has made use of the SIMBAD database, operated at CDS, Strasbourg, France (Wenger et al. 2000) and the VizieR catalogue access tool, CDS, Strasbourg, France (DOI: 10.26093/cds/vizier). The original description of the VizieR service was published in Ochsenbein et al. (2000).

Some of the authors benefited from grant No. 863448 (NEANIAS) of the Horizon 2020 European Commission programme. H.A. benefited from grant CIIC 90/2020 of Universidad de Guanajuato, Mexico. M.J.M. acknowledges the support of the National Science Centre, Poland through the SONATA BIS grant 2018/30/E/ST9/00208.

DATA AVAILABILITY

Source tables are provided as online supplementary material.

The following catalogue data products are available in the Zenodo repository[25] at `http://doi.org/10.5281/zenodo.4386692`:

(i) **Source catalogue in tabular format**: Two ascii/FITS table files with a series of summary parameters for each catalogued source islands and fitted components, respectively. Table format (number of data columns and column description) is detailed in the CAESAR documentation at `https://caesar-doc.readthedocs.io`. Additionally, we provide an added-value source component catalogue table (ascii and FITS formats) with extra-information (corrected fluxes, radio/infrared cross-match info, spectral indices, etc.). Its format is described in Table B1 (available in the online version of this paper)

(ii) **Source catalogue in Root format**: A ROOT[26] file storing the list of catalogued sources and relative components as a CAESAR `Source` C++ object. For each source the summary parameters plus detailed information at pixel level are available. The detailed format is described in the CAESAR API documentation at `https://caesar-doc.readthedocs.io`.

(iii) **Source list in region format**: Two DS9[27] region files with the list of catalogued source islands and fitted components, respectively reported as labelled polygons or ellipses.

(iv) **Background maps in FITS format**: Two FITS files with background and noise maps obtained in the source finding process.

[25] `https://zenodo.org/`

[26] `https://root.cern.ch/`

[27] `http://ds9.si.edu/`

REFERENCES

Anderson, C., et al. [ACES and SDP teams], *ASKAP Science Observation Guide*, CSIRO, version 1.1, July 2019
Anglada, G., et al., 1998, AJ, 116, 2953
Anglada, G., et al., 2018, Astron Astrophys Rev, 26, 3
Ainsworth, R. E., et al. (AMI Consortium), 2012, MNRAS, 423, 1089
Akras, S., et al., 2019, MNRAS, 488, 3238
Anderson, L. D., et al., 2012, A&A, 537, A1
Anderson, L. D., et al., 2014, APJSS, 212, 1
Assef,R. J., et al., 2018, ApJS, 234, 23
Astropy Collaboration, Robitaille T. P., Tollerud E. J., Greenfield P., Droettboom M., Bray E., Aldcroft T., et al., 2013, A&A, 558, A33
Astropy Collaboration, Price-Whelan A. M., Sipőcz B. M., Günther H. M., Lim P. L., Crawford S. M., Conseil S., et al., 2018, AJ, 156, 123
Brown, A. G.A. et al. (Gaia collaboration), 2018, A&A, 616, A1
Brun, R. and Rademakers, F., Proc. AIHENP'96 Workshop, Lausanne, Sep. 1996, Nucl. Inst. & Meth. in Phys. Res. A, 389 (1997) 81
Butler, A., et al., 2018, A&A 620, A3
Caswell, J. L., Haynes R. F., 1983, AuJPh, 36, 361
Cavallaro, F., et al., 2018, MNRAS, 473, 1685
Chang, C., et al., 2008, ApJ, 682, 1177
Churchwell, E., et al., 2009, PASP, 121, 877
Clarke, A. O., et al., 2020, A&A, 639, A84
Condon, J. J., 1997, PASP, 109, 166
Condon, J. J., 1984, AJ, 287, 461.
Condon, J. J., et al., 1998, AJ, 115, 1693
Condon, J. J., Kaplan, D. L., 1998, ApJS, 117, 361
Cutri, R. M., Wright, E. L., Conrow, T., et al. 2013, Explanatory Supplement to the AllWISE Data Release Products, Tech. rep.
Dale, D. A., et al., 2012, ApJ, 745, 95
Franzen, T. M. O., et al., 2015, MNRAS, 453, 4020
Franzen, T. M. O., et al., 2019, PASA, 36, E004
Fragkou, V., et al., 2018, MNRAS, 480, 2916
Gaylard, M. J., MacLeod, G. C., 1993, MNRAS, 262, 43
Green, D. A., 2019, Journal of Astrophysics and Astronomy, 40, 36.
Han, J., et al., 2016, Res. Astron. Astrophys., 16, 159
Hopkins, A. M., et al., 2015, PASA, 32, E037
Hopkins, A. M. et al., 2003, AJ, 125, 465
Hurley-Walker, N., et al., 2017, MNRAS, 464, 1146
Hurley-Walker, N., et al., 2019, PASA, 36, E047
Iglesias-Páramo J., et al., 2007, ApJ, 670, 279
Ingallinera, A., et al., 2014, MNRAS, 437, 3626
Ingallinera, A., et al., 2017, Proc. of the International Astronomical Union, 12 (S331), 345-350, doi: `https://doi.org/10.1017/S1743921317004574`
Ingallinera, A., et al., 2019, MNRAS, 490, 5063

Intema, H. T., et al., 2017, A&A, 598, A78
Jankowski, F., et al., 2018, MNRAS, 473, 4436
Jankowski, F., et al., 2019, MNRAS, 484, 3691
Jeyakumar, S., 2016, MNRAS, 458, 3786
Johnston, S., Kerr, M., 2018, MNRAS, 474, 4629.
Johnston, S., et al., 2008, Experimental Astronomy, 22, 151
Johnston, S., et al., 1992, MNRAS, 255, 401
Joye, W. A., Mandel, E., 2003, in Astronomical Data Analysis Software and Systems XII, eds. H. E. Payne, R. I. Jedrzejewski, & R. N. Hook, ASP Conf. Ser., 295, 489
Katgert, P., Oort, M. J. A., & Windhorst, R. A., 1988, A&A, 195, 21
Kimball, A. E. and Ivezić, Ž., 2008, AJ, 136, 684
Kramer, M., et al, 2003, MNRAS, 342, 1299
Kwok, S., 2000, The Origin and Evolution of Planetary Nebulae. Cambridge University Press
Lacy, M., et al., 2020, PASP, 132, 035001
Leto, P., et al., 2006, A&A, 458, 831
Leto, P., et al., 2017, MNRAS, 467, 2820
Leto, P., et al., 2018, MNRAS, 476, 562
Manchester, R. N., Hobbs, G. B., Teoh, A., & Hobbs, M., 2005, AJ, 129, 1993
Maron, O., et al., 2000, A&A, 147, 195
Molinari, S., et al., 2016, A&A, 591, A149
Murphy, T., et al., 2007 , MNRAS, 382, 382
McConnell, D., et al., 2016, PASA, 33, e042
Michałowski M. J., et al., 2008, ApJ, 672, 817
Michałowski M., et al., 2010, A&A, 514, A67
Milne, D. K., Aller, L. H., 1975, A&A, 38, 183
Milne, D. K., Aller, L. H., 1982, A&AS, 50, 209
Nikutta, R., et al., 2014, MNRAS, 442, 3361
Norris, R. P., et al., 2011, PASA, 28, 215
Ochsenbein, F., Bauer, P., Marcout, J., 2000, A&AS, 143, 23
Ofek, E. O., Frail, D. A., 2011, ApJ, 737, 45
Parker, Q. A. et al, 2016, J. Phys. Conf. Ser., 728, 032008
Pilbratt, G. L., et al., 2010, A&A, 518, L1
Pottasch, S. R., Planetary nebulae - A study of late stages of stellar evolution, by S.R. Pottasch. Dordrecht, D. Reidel Publishing Co. (Astrophysics and Space Science Library. Volume 107), 1984, 335 p.
Prandoni, I., et al, 2001, A&A, 365, 392
Purcell,C. R., et al., 2013, ApJS, 205, 1
Retana-Montenegro, E., et al, 2018, A&A, 620, A74
Reynolds, S. P., 1986, ApJ, 304, 713
Riggi, S., et al., 2016, MNRAS, 460, 1486
Riggi, S., et al., 2019, PASA, 36, E037
Robitaille, T., Bressert, E., 2012, APLpy: Astronomical Plotting Library in Python, Astrophysics Source Code Library (ascl:1208.017)
Rosslowe, C. K., Crowther, P. A., 2015, MNRAS, 447, 2322
Scaife, A.M. M., 2012, Astronomical Review, 7, 26
Schinckel, A. E., et al, 2012, in Ground-based and Airborne Telescopes IV. p. 84442A, doi:10.1117/12.926959
Silva, L., et al., 1998, ApJ, 509, 103
Suarez, O. et al, 2006, A&A, 458, 174
Taylor, M. B., 2005, in Shopbell P., Britton M., Ebert R., eds, Astronomical Society of the Pacific Conference Series Vol. 347, Astronomical Data Analysis Software and Systems XIV. p. 29
Taylor, M., 2011, TOPCAT: Tool for OPerations on Catalogues And Tables, Astrophysics Source Code Library (ascl:1101.010)
Thorat, K., et al, 2013, ApJ, 762, 16
Umana, G., et al., 2015, MNRAS, 454, 902
Umana, G., et al., 2020, in prep.
Urquhart, J. S., et al., 2009, A&A, 501, 539
Urquhart, J. S., et al., 2018, MNRAS, 473, 1059
van de Steene, G. C. M, Pottasch, S. R., 1993, A&A, 274, 895
Wang, Y., et al, 2018, A&A, 619, A124
Wendker, H. J., 1995, A&AS, 109, 177; March 2001 update of the catalogue, CDS VIII/99
Wenger, M., et al., 2000, A&AS, 143, 9
Werner, M. W., et al., 2004, ApJS, 154, 1
Wilson, W. E., et al., 2011, MNRAS, 416, 832
Windhorst, R., et al, 1990, in Evolution of the Universe of Galaxies: Edwin Hubble Centennial Symposium, ed. R. G. Kron, ASP Conf. Ser., 10, 389
Whiting, M., et al., ASKAP Science Data Processor software, https://bitbucket.csiro.au/scm/casssoft/askapsoft.git
Wright, E. L., et al., 2010, AJ, 140, 1868
Zajaček, M., et al., 2019, A&A, 630, A83
Zhang, Y, et al., 2004, MNRAS, 351, 935
Zhao, R. S., et ak., 2019, ApJ, 874, 64